



LUND UNIVERSITY
Faculty of Science

Time-resolved x-ray diffraction study of longitudinal optical phonons in zincblende semiconductors

Lassi Linnala

Thesis submitted for the degree of Master of Science
Project duration: 4.5 months

Supervisor: Jörgen Larsson
Co-Supervisor: Eric Nilsson

Department of Physics
Division of Atomic Physics
June 2021

Abstract

Anharmonic decay of longitudinal optical (LO) phonons in zincblende semiconductors is not at present well characterized due to the polar and many-body nature of the problem. Femtosecond THz radiation offers a novel route to this study, as the interaction of this radiation is directly with the phonon lattice and these THz excited phonons do not have enough energy to excite electrons over the band gap. Therefore, their decay is entirely due to anharmonic interactions with other phonon modes in the lattice. In this thesis, it has been hypothesized that by the correct choice of THz polarization and for achievable THz field strengths, the atomic motion in the THz excited LO phonon modes and their decay could be directly observed as an intensity modulation of the nearly forbidden reflections of the zincblende structure with time-resolved x-ray diffraction (TXRD). In the framework of an ultrafast THz pump, TXRD probe experiment, this thesis consists of investigating this hypothesis using a theoretical model.

Modelling the LO phonons as harmonic oscillators driven by the electric fields of the THz radiation and where the material parameters have been simulated using density functional perturbation theory for InSb. The results show that for a 200 fs Gaussian THz pulse centered at the LO phonon frequency, 20% increase in the TXRD intensity can already be observed for a THz field strength of 0.3 MV/cm. Due to the anharmonic decay of the LO phonon, significant intensity modulation can be observed even 10 ps after the THz pulse. These results on InSb suggest that if THz radiation can be generated close to the LO phonon frequency, significant TXRD intensity modulation can be observed in any zincblende semiconductor for achievable THz field strengths. Therefore, the present thesis paves a way for a new ultrafast time-resolved technique to measure the anharmonic lifetimes of LO phonons in zincblende semiconductors, for which the data is at present lacking, and which are needed for the advancement of hot carrier solar cells.

Acknowledgements

I want to thank my supervisor Prof. Jörgen Larsson for his excellent idea for a Master's project and his patient supervision. I thank him also for introducing me to the exciting field and to the capabilities of ultrafast pump-probe experiments. I further extend my gratitude to my co-supervisor Eric Nilsson and the entire ultrafast x-ray science group.

I also thank Prof. Ferdi Aryasetiawan for his help and insights on group theory and electronic structure theory. Final thanks goes to the ABINIT group for their excellent tutorials on how to use the ABINIT code for density functional (perturbation) theory simulations, without which the present simulations would have been difficult.

Contents

Abbreviations	iv
1 Introduction	1
2 Scientific Background	5
2.1 Crystal structure and x-ray diffraction	5
2.1.1 Real and reciprocal space of zincblende InSb	6
2.1.2 Nearly forbidden Bragg reflections of zincblende	7
2.1.3 Atomic form factors of In and Sb	8
2.2 Theory of phonons	9
2.2.1 Dynamical matrix in the harmonic approximation	9
2.2.2 Anharmonic decay of phonons	10
2.2.3 Group theory of phonons in zincblende	12
3 Theoretical Methods	15
3.1 Harmonic oscillator model for the THz excited phonons	16
3.2 Density functional theory	18
3.2.1 Self-consistent Kohn-Sham equations	19
3.2.2 Exchange and correlation functional	20
3.2.3 Plane waves and pseudopotentials	21
3.2.4 Brillouin zone sampling	22
3.2.5 Self-interaction error and the electron structure of InSb	23
3.3 Density functional perturbation theory	25
3.3.1 Phonons, linear and non-linear optics of polar semiconductors	26
4 Results and Discussion	27
4.1 Longitudinal optical phonons in InSb for the THz excitation	28
4.2 Linear and non-linear optical responses of InSb	31
4.3 Time-resolved x-ray diffraction of THz excited LO phonons	31
4.4 Preliminary experimental results from FemtoMAX	39
5 Conclusion and Outlook	39
References	41
Appendices	49
A Coefficients for the atomic form factors of In and Sb	49
B Group theory of zincblende	49
C Computational details for DFPT	53
D Exchange interaction in the homogeneous electron gas	54
E Optical phonons in polar semiconductors	56

Abbreviations

TXRD	-	Time-resolved X-Ray Diffraction
LO	-	Longitudinal Optic
LA	-	Longitudinal Acoustic
TO	-	Transverse Optic
TA	-	Transverse Acoustic
FWHM	-	Full Width at Half Maximum
DFPT	-	Density Functional Perturbation Theory
BZ	-	Brillouin Zone
IBZ	-	Irreducible Brillouin Zone
FC	-	Force Constant
rep	-	Representation
irrep	-	Irreducible Representation
DFT	-	Density Functional Theory
KS	-	Kohn-Sham
XC	-	Exchange and Correlation
SIE	-	Self-Interaction Error
HFA	-	Hartree-Fock Approximation
LDA	-	Local Density Approximation
GGA	-	Generalized Gradient Approximation
HGH	-	Hartwigsen-Goedecker-Hutter

1 Introduction

The advent of ultrafast pump-probe experiments has given us an unique insight into various properties of the condensed matter, such as the study of structural dynamics in solids.^[1-4] In such studies, typically an optical femtosecond laser is used to pump the solid into an excited state and the relaxation is probed with a structurally sensitive technique, such as ultrafast time-resolved x-ray diffraction (TXRD). In these optical femtosecond laser pump, x-ray probe experiments, the optical radiation initially excites the electronic system which then equilibrates with the phonon lattice via various electron-phonon and phonon-phonon coupling mechanisms. These coupling mechanisms allow for generation of coherent lattice vibrations which can be observed with x-ray diffraction, and their decay can be further studied. For example, by probing the strain caused by coherent acoustic phonons which affects the Bragg angle.^[5-10]

In contrast to the optical lasers, femtosecond THz radiation offers a novel route to the study of optical phonons in semiconductors as this radiation does not heat the crystal and its interaction is directly with the phonon lattice. These THz excited phonons do not have enough energy to excite electrons over the band gap and their decay is, therefore, entirely due to interactions with other phonon modes in the lattice. This is also known as the anharmonic decay, in which a THz excited zone center optical phonon, $q \sim 0$, decays into two other phonons of opposite momenta, $q' = -q''$, conserving energy.

It is important to distinguish that the anharmonic decay of the near zone center optical phonons can result in phonons of various wave vectors and this decay does not favor small wave vector phonons.^[11] This is unlike the phonons that are directly emitted by the optical laser excited small wave vector conduction electrons. Therefore, it would be difficult to gain full information on the anharmonic decay of the optical phonons by probing, for example, the acoustic phonons that result from the decay with x-rays. Unless, all the channels in the entire Brillouin zone can be resolved at once.

The different electron-phonon coupling mechanisms of an optical laser excited conduction electrons have been highlighted in Fig. 1 for a polar semiconductor. Acoustic or specifically longitudinal acoustic (LA) phonons can be generated via piezoelectric or deformation potential coupling, respectively, and these phonons will be restricted to small wave vectors, $q \sim 0$, if only intraband scattering is considered.^[12] The figure also highlights the THz excitation of longitudinal optical (LO) phonons, which are also connected to the electron lattice via the Fröhlich coupling.^[13] These THz or Fröhlich excited small wave vector LO phonons decay anharmonically into two other phonons of opposite momenta, $q' = -q''$, throughout the Brillouin zone.

In polar semiconductors, the anharmonic decay of LO phonons is the fundamental mechanism for carrier energy relaxation, as these phonons are connected to the electron lattice via the strong Fröhlich coupling. For example in zincblende InSb, the prototype material used in this thesis, the lifetime of a thermal electron at room temperature due to this coupling is ~ 2 ps.^[14] In comparison, the lifetime of the same electron due to the deformation potential coupling to LA phonons is ~ 11 ps.^[14] Thus, if electrons are excited in polar semiconductors they will emit LO phonons. These LO phonons will then either couple back to the conduction electrons, or anharmonically decay into other phonons.

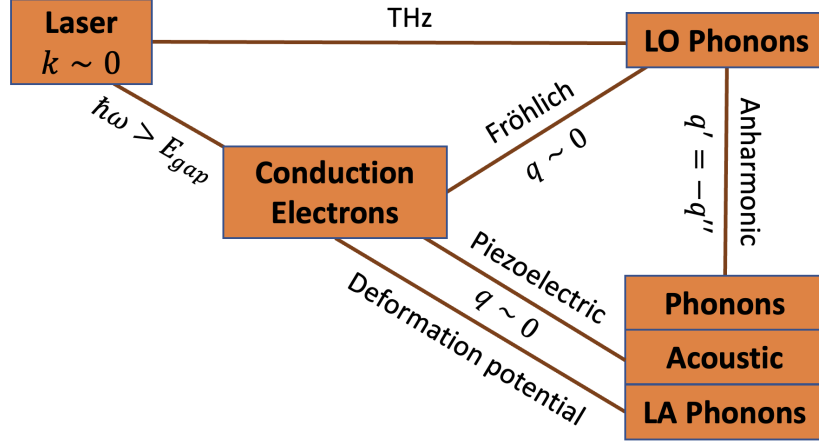


Figure 1: Ultrashort optical and THz laser excitation of coherent phonons and the fundamental carrier energy relaxation mechanisms in polar semiconductors,^[12,14–16] as discussed in the text.

Therefore, the anharmonic decay of the LO phonons is an important material parameter for modelling the energy relaxations and to the design of semiconductor devices using these polar semiconductors. In particular, data on the anharmonic lifetimes of the polar LO phonons are needed to realize the phonon bottleneck.^[17] This bottleneck slows down the hot carrier thermalization via the Fröhlich emission of LO phonons and their subsequent anharmonic decay, and which is the fundamental requirement for the advancement of hot carrier solar cells that promise efficiency beyond the Shockley–Queisser limit.^[18–20]

Anharmonic decay of non-equilibrium (near) zone center LO phonons in polar semiconductors has been studied over five decades.^[17] Still, there is no general technique for determining the different phonons involved in the decay^[11,21–24] or the lifetimes in different materials,^[17] which further show strong temperature dependence.^[11,22] In particular, for InSb the data is at present contradicting. Ferry^[25] has calculated 7.26 ps lifetime for the LO phonon in InSb at 300 K, under the assumption that the only decay channel for the LO phonon is into two LA phonons of equal frequency. This decay channel is known as the Klemens channel.^[21] By studying diffuse x-ray scattering in InSb after an ultrashort optical laser excitation, Trigo et al.^[26] observed excitation of transverse acoustic (TA) phonons throughout the Brillouin zone. This could indicate that the anharmonic decay of the LO phonon in InSb is more dominantly into a TA and, for example, a transverse optic (TO) phonon, instead of the commonly assumed Klemens channel. However, Trigo et al. have been limited to dynamics that occur on a larger time scale than 100 ps due to their x-ray pulse duration. Therefore, their observed TA phonons can result from the further decay of the decay products of the initially Fröhlich excited LO phonons.

If the study of the different decay channels is neglected, the Lorentzian lineshape of a Raman peak is inherently broadened by the anharmonic lifetime of the corresponding phonon mode. Cardona et al.^[27] have measured the Raman spectrum of InSb and based on this measurement, approximately 6 ps lifetime for the LO mode can be extracted. However, it is difficult to determine the Lorentzian full width at half maximum (FWHM) from Raman spectra due to other broadening mechanisms. The decay rate of an optical phonon mode can also be fitted from reflectance spectra via the Kramers-Kronig relations

using a model dielectric function that contains a damping parameter.^[28] By performing this study, Palik^[29] has reported 12 ps lifetime for both the LO and TO modes in InSb at room temperature. The lifetimes of these two modes should, however, be fundamentally different due to the polar nature of the LO phonon and also the resulting LO-TO splitting in ionic crystals.^[28] Lockwood et al.^[30] have improved the model and determined 10 ps lifetime for the LO mode in InSb with the same technique.

In this thesis, we report a theoretical modelling of an ultrafast THz pump, TXRD probe experiment to study the anharmonic lifetime of the LO phonon in zincblende InSb. This theoretical model serves as a tool to study the feasibility and to gain insight into such pioneering experiment at the pump-probe beamline FEMTO-MAX^[31] at MAX IV synchrotron radiation facility. The initial idea of this experiment is to excite a coherent LO phonon mode in InSb by choosing the polarization of the THz pump laser along the In and Sb bond direction as shown in Fig. 2(a). The electric field of the THz radiation will then excite a dipole active LO phonon mode, where the In lattice (brown atoms) oscillates against the Sb lattice (purple atoms), as highlighted by the green arrows.

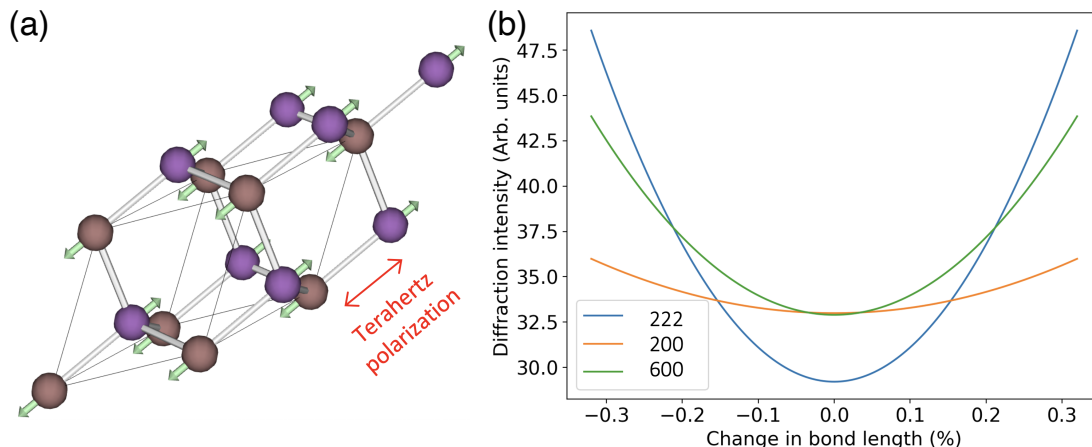


Figure 2: Phonon mode in InSb and the resulting modulation of XRD intensity: (a) THz excitation of a LO phonon mode in InSb, where the In (brown) and Sb (purple) lattices oscillate against each other, as denoted by the green arrows. (b) XRD intensity modulation of the nearly forbidden reflections: {222, 200, 600} of InSb, when the bond length between In and Sb varies along the phonon mode shown in (a). Phonon mode in (a) has been visualized using.^[32]

Zincblende crystal structure of InSb hosts a set of nearly forbidden Bragg reflections,^[33] {222, 200, 600}, where the diffraction intensity is proportional to the difference of the atomic form factors of In and Sb, $I \propto |f_{\text{In}} - f_{\text{Sb}}|^2$. These form factors are related to the atomic numbers of the atoms and as In and Sb are close to each other in the periodic table, the diffraction intensity of these reflections is very weak in the equilibrium geometry.

The existence of these nearly forbidden Bragg reflections in the zincblende structure allows us to directly observe the motion of the atoms in the THz excited LO phonon mode with TXRD, provided that large enough oscillation amplitudes can be excited by the electric fields of the THz radiation. The theoretical XRD intensity modulation has been plotted in Fig. 2(b), which results from displacing the In and Sb atoms along the phonon mode shown in Fig. 2(a). It is seen that approximately 20% increase in the

intensity of the 222 reflection can be observed, if the bond length between the In and Sb atoms increases or decreases by 0.2%.

Once the LO phonon mode has been excited, the lattice then oscillates around its equilibrium position and anharmonically decays into other phonons. This oscillation and decay causes both a periodic modulation and a decay of the TXRD intensity back to its equilibrium value. By monitoring this modulation and its decay with TXRD on a sub-picosecond time scale allows to fit the anharmonic lifetime of the phonon mode from the experimental data using a theoretical model, which is also used to model the experiment.

In this theoretical model, the displacements of the atoms in the THz excited phonon mode with frequency ω_0 are modelled with driven damped harmonic oscillator equations,

$$\left(\frac{\partial^2}{\partial t^2} + 2\Gamma\frac{\partial}{\partial t} + \omega_0^2\right)u_{m,i}(t) = \frac{F_{m,i}(t)}{M_m}, \quad (1.1)$$

where $u_{m,i}$ is the displacement of an atom m with mass M_m in a Cartesian direction i due to the force $F_{m,i}$ exerted by the electric fields of the THz pulse. The damping parameter is inverse proportional to the anharmonic lifetime, τ , of the phonon mode, $2\Gamma = 1/\tau$.

These displacements can then be inserted into the structure factor,^[33]

$$F_{hkl}(t) = \sum_m f_m e^{2\pi i[hx_m(t)+ky_m(t)+lz_m(t)]}, \quad (1.2)$$

where f_m is the atomic form factor of an atom m and the Cartesian positions of the atoms can be taken to contain both their equilibrium positions, $r_{m,i}$, and their displacements, e.g., $x_m(t) = r_{m,x} + u_{m,x}(t)$, (in units of the lattice constant). The TXRD intensity of a reflection hkl is then given as $I_{hkl}(t) = |F_{hkl}(t)|^2$.

Major task in the present thesis is to determine the force term and the phonon modes for the above harmonic oscillator model. This force term depends on the electric fields of the femtosecond THz laser pulse and the material parameters of InSb that describe its response to external electric fields. In this thesis, these material parameters are simulated from first-principles using density functional perturbation theory (DFPT). DFPT also gives us the phonon dispersion and the phonon modes of InSb, which allows us to first identify the LO phonon mode shown in Fig. 2(a), and to further consider other LO phonon modes and their effect on the TXRD intensity as well.

The present thesis provides a connection between TXRD and the anharmonic decay of the (near) zone center LO phonon modes in zincblende semiconductors. The harmonic oscillator model built from first-principles allows us to model the feasibility and to gain insight into how to best perform such pioneering experiment. This model also serves as a tool to determine the LO phonon anharmonic lifetime from future experimental data. While the present work specifically considers InSb due to its optical phonon frequencies being close to the femtosecond THz frequencies that can be generated from DAST organic crystal^[34] at the FemtoMAX beamline. The technique described here can be extended to other zincblende semiconductors as well. In particular, the results on InSb suggest that if THz radiation can be generated close to the resonance frequency of the LO phonon, significant intensity modulation in any of the nearly forbidden reflections in any polar zincblende semiconductor for moderate THz field strengths can be observed. Therefore,

the present thesis paves a way for a new ultrafast time-resolved technique to characterize the anharmonic lifetimes of the LO phonons in different zincblende semiconductors. For which the data is at the present lacking, and which are needed as material parameters for modelling the carrier energy relaxations in the search of materials for hot carrier solar cells beyond the Shockley-Queisser limit.

2 Scientific Background

In this section the theoretical framework for the present thesis is reviewed. First, the real and reciprocal space of crystalline solids is described, and it is made clear how these two are connected via XRD. Then, the zincblende structure of InSb is characterized, which allows to derive the selection rules for the Bragg reflections of the zincblende structure and express their intensities in terms of atomic form factors. These form factors are then quantified for In and Sb which are needed for modelling the TXRD intensity.

After the description of crystal structure and XRD, the theory of phonons is reviewed. First in harmonic approximation and then at anharmonic level, as given by Taylor expanding the crystal potential. The harmonic approximation gives the theoretical framework to understand and to simulate phonons with DFPT, while the anharmonic terms describe their decay. In the final section, the phonons in zincblende are discussed in terms of group theory, which allows to determine their selection rules for the THz excitation, and which is needed for constructing the force term for the harmonic oscillator model.

2.1 Crystal structure and x-ray diffraction

Position vector of an atom l in unit cell n of a crystalline material can be written as,

$$\mathbf{R}_{ln} = \mathbf{r}_l + \mathbf{T}_n, \quad (2.1)$$

where \mathbf{r}_l is the equilibrium position of atom l in the primitive unit cell. The translation vector of the underlying Bravais lattice is,

$$\mathbf{T}_n = n_1 \mathbf{a}_1 + n_2 \mathbf{a}_2 + n_3 \mathbf{a}_3, \quad (2.2)$$

where n_i are integers and which together with primitive lattice translation vectors, \mathbf{a}_i , span the Bravais lattice. The entire crystalline structure can be generated by translating the basis atoms at positions \mathbf{r}_l by this vector.

Scattering of x-rays from crystalline solids can be described by the structure factor,^[35]

$$F(\mathbf{q}) = \sum_n e^{i\mathbf{q}\cdot\mathbf{T}_n} \sum_l f_l(\mathbf{q}) e^{i\mathbf{q}\cdot\mathbf{r}_l}, \quad (2.3)$$

where $\mathbf{q} = \mathbf{k} - \mathbf{k}_0$ is the scattering vector, and the momenta of the incident \mathbf{k}_0 and scattered radiation \mathbf{k} have been assumed to be equal, $|\mathbf{k}| = |\mathbf{k}_0| = 2\pi/\lambda$, i.e., the scattering is elastic. For x-ray scattering from atoms, the atomic form factor $f_l(\mathbf{q})$ is given by Fourier transform of the electron density of the atom l , which will be quantified in Sec. 2.1.3.

In the structure factor, the first sum describes the scattering entirely from the underlying Bravais lattice, characterized by \mathbf{T}_n , while the second sum describes the scattering from the basis atoms at positions \mathbf{r}_l . This structure factor gives the intensity of the scattering as $I(\mathbf{q}) = |F(\mathbf{q})|^2$. For diffraction, it is of interest to discuss for which scattering vectors \mathbf{q} this intensity is maximized. Clearly, if in the first sum $\exp(i\mathbf{q} \cdot \mathbf{T}_n) = 1$, then the sum over n primitive unit cells in a macroscopic crystal is large. Therefore, the diffraction occurs for scattering vectors that satisfy, $\mathbf{q} \cdot \mathbf{T}_n = 2\pi \times \text{integer}$. The set of such scattering vectors can be defined as the reciprocal lattice translation vector,

$$\mathbf{G}_{hkl} = h\mathbf{b}_1 + k\mathbf{b}_2 + l\mathbf{b}_3, \quad (2.4)$$

where hkl are integers, which together with the reciprocal space primitive lattice translation vectors, \mathbf{b}_i , span the reciprocal lattice. The integers hkl are the Miller indices and, as diffraction occurs at different reciprocal lattice vectors, they label the reflections.

The above described condition, that diffraction occurs if the scattering vector satisfies $\mathbf{q} = \mathbf{k} - \mathbf{k}_0 = \mathbf{G}_{hkl}$, tells us that x-ray diffraction probes the reciprocal lattice of a crystalline solid. This is known as the Laue condition of diffraction and from which the reciprocal space can be constructed more explicitly. It was defined that,

$$\mathbf{G}_{hkl} \cdot \mathbf{T}_n = 2\pi \times \text{integer}. \quad (2.5)$$

Therefore, the primitive components of the real and reciprocal lattices satisfy,

$$\mathbf{a}_i \cdot \mathbf{b}_j = 2\pi\delta_{ij}. \quad (2.6)$$

This is satisfied by cyclic permutations of subscripts of the construction,

$$\mathbf{b}_1 = \frac{2\pi}{\Omega_0}(\mathbf{a}_2 \times \mathbf{a}_3), \quad (2.7)$$

where the volume of the real space primitive unit cell is given by $\Omega_0 = |\mathbf{a}_1 \cdot (\mathbf{a}_2 \times \mathbf{a}_3)|$.

2.1.1 Real and reciprocal space of zincblende InSb

The zincblende crystal structure of InSb consists of two atoms per primitive unit cell at positions $\mathbf{r}_{\text{In}} = [0, 0, 0]$ and $\mathbf{r}_{\text{Sb}} = [1, 1, 1]a/4$, and the fcc primitive lattice vectors,

$$\mathbf{a}_{\text{fcc}} = \begin{bmatrix} \mathbf{a}_1 \\ \mathbf{a}_2 \\ \mathbf{a}_3 \end{bmatrix} = a \begin{bmatrix} 0 & 1/2 & 1/2 \\ 1/2 & 0 & 1/2 \\ 1/2 & 1/2 & 0 \end{bmatrix} \begin{bmatrix} x \\ y \\ z \end{bmatrix}, \quad (2.8)$$

where a is the cubic lattice constant and which for InSb is $a = 6.4793 \text{ \AA}$ at 293 K.^[36]

Using (2.7), the primitive reciprocal lattice vectors can be constructed from (2.8) as,

$$\mathbf{b}_{\text{bcc}} = \begin{bmatrix} \mathbf{b}_1 \\ \mathbf{b}_2 \\ \mathbf{b}_3 \end{bmatrix} = \frac{2\pi}{a} \begin{bmatrix} -1 & 1 & 1 \\ 1 & -1 & 1 \\ 1 & 1 & -1 \end{bmatrix} \begin{bmatrix} x \\ y \\ z \end{bmatrix}, \quad (2.9)$$

which correspond to a bcc lattice.

The cubic conventional unit cell of the zincblende InSb with lattice constant a is shown in Fig. 3(a), where the In atoms are shown in brown and Sb atoms in purple. The primitive unit cell with the two atom basis is also highlighted by the fcc primitive translation vectors \mathbf{a}_i . This zincblende structure can be thought as two distinct fcc lattices formed by the In and Sb atoms which are shifted by $[1, 1, 1]a/4$ from each other.

In Fig. 3(b) is shown the Wigner-Seitz cell of a bcc lattice, which can be defined as the primitive reciprocal space unit cell of zincblende InSb. This cell also defines the first Brillouin zone (BZ). In the figure are also marked the high-symmetry points, which arise from the point symmetries of the crystal. The area enclosed by these points forms the irreducible Brillouin zone (IBZ), which is important as properties of solids, such as the phonon modes, can be entirely in described this region.

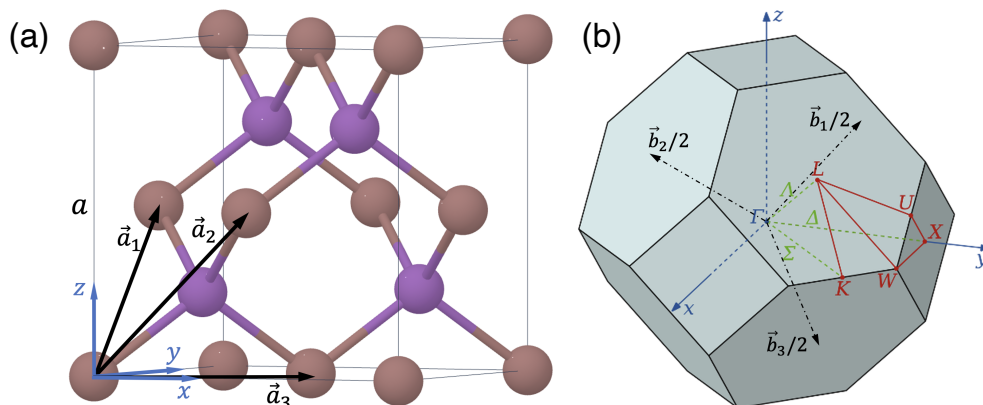


Figure 3: Real and reciprocal lattice of zincblende InSb: (a) Conventional unit cell with lattice constant a and the primitive unit cell denoted by the primitive vectors \mathbf{a}_i . (b) Brillouin zone of InSb, where the area enclosed by the high-symmetry points forms the irreducible Brillouin zone.

2.1.2 Nearly forbidden Bragg reflections of zincblende

The conventional unit cell of InSb consists of four In atoms at Cartesian positions,

$$\text{In: } \begin{bmatrix} 0 & 0 & 0 \\ 0 & \frac{1}{2} & \frac{1}{2} \\ \frac{1}{2} & 0 & \frac{1}{2} \\ \frac{1}{2} & \frac{1}{2} & 0 \end{bmatrix}, \quad (2.10)$$

and four Sb atoms shifted by $1/4[1, 1, 1]$. Summing over these In and Sb atoms in the conventional unit cell, the structure factor in (1.2) becomes,

$$F_{hkl}^{\text{InSb}} = (1 + e^{\pi i(k+l)} + e^{\pi i(h+l)} + e^{\pi i(h+k)}) \times (f_{\text{In}} + f_{\text{Sb}} e^{\pi i(h+k+l)/2}). \quad (2.11)$$

This can be determined to give the following selection rules for the reflections hkl ,^[33]

$$F_{hkl}^{\text{InSb}} = \begin{cases} 4(f_{\text{In}} + f_{\text{Sb}}) & h + k + l = 4N, \\ 4(f_{\text{In}} \pm i f_{\text{Sb}}) & h + k + l = 2N + 1, \\ 4(f_{\text{In}} - f_{\text{Sb}}) & h + k + l = 4N + 2, \end{cases} \quad (2.12)$$

where N is an integer.

The atomic form factors, f_{In} and f_{Sb} , were described to be given by the Fourier transform of electron density of the corresponding atom. For In and Sb with atomic numbers $Z = 49$ and $Z = 51$, respectively, the form factors are almost equal. Therefore, as the intensity for the set of reflections $h+k+l = 4N+2$ is given by $I_{hkl} = |F_{hkl}|^2 = |4(f_{\text{In}} - f_{\text{Sb}})|^2$, the set of reflections: $\{222, \bar{2}\bar{2}\bar{2}, 200, 600\}$ are weak in equilibrium.

2.1.3 Atomic form factors of In and Sb

To model the TXRD intensity, it is necessary to quantify the atomic form factors. Considerable computational effort has gone into accurately determining electron density of atoms in the periodic table from the best known wave functions. Using relativistic Hartree-Fock or Dirac-Slater wave functions, the form factors have been calculated in Ref.^[37] For convenience, the authors have parametrized the form factors as a sum of Gaussians,

$$f(q) = \sum_{i=1}^4 a_i \exp\left(-b_i \left(\frac{q}{4\pi}\right)^2\right) + c, \quad (2.13)$$

where the coefficients, a_i , b_i and c , for In and Sb have been tabulated in appendix A.

The atomic form factors of In and Sb have been plotted in Fig. 4(a) as a function of magnitude of the scattering vector $q = |\mathbf{k} - \mathbf{k}_0|$. The scattering lengths of the different nearly forbidden reflections: $q_{hkl} = |\mathbf{G}_{hkl}| = 2k_0 \sin \theta$, where θ is the Bragg angle,^[28] have also been denoted on the x -axis. At $q = 0$, the difference between the form factors is the difference between their atomic numbers, 49 and 51. This difference is almost constant over the whole plotted scattering range. Therefore, the intensities of the different nearly forbidden reflections, given by the difference of the atomic form factors at the different scattering lengths, are almost identical in the equilibrium geometry.

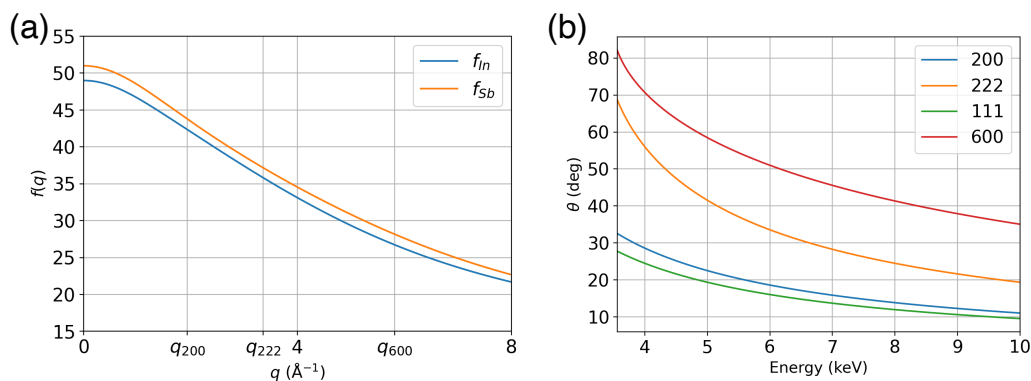


Figure 4: (a) Atomic form factors of In and Sb as a function of $q = |\mathbf{k} - \mathbf{k}_0|$ where the scattering lengths of the different nearly forbidden reflections, $q_{hkl} = |\mathbf{G}_{hkl}|$, are denoted on the x -axis. (b) Bragg angles of different reflections as a function of x-ray energy.

In Fig. 4(b) are shown the Bragg angles of different reflections as a function of x-ray energy. These angles give constraints for probing the different reflections experimentally. For example, as the 600 diffracts at large angles, it might be more difficult to realize an experimental geometry for this reflection, unless high fluxes of hard x-rays are available.

2.2 Theory of phonons

The theoretical framework for phonons can be formulated around the force constants arising from the Taylor expansion of the crystal potential.

If the previous definition of the position of an atom l in the primitive unit cell n is extended to also contain a displacement \mathbf{u}_{ln} ,

$$\mathbf{R}_{ln} = \mathbf{r}_l + \mathbf{T}_n + \mathbf{u}_{ln}. \quad (2.14)$$

The potential energy E of a crystal can then be expanded as a Taylor series for these displacements in Cartesian directions, denoted by the Greek letters $\alpha\beta\gamma$, as,^[38]

$$\begin{aligned} E(\{\mathbf{u}\}) = E_0 &+ \sum_{ln\alpha} \Phi_{ln\alpha} u_{ln\alpha} + \frac{1}{2!} \sum_{ln\alpha} \sum_{l'n'\beta} \Phi_{ln\alpha}^{l'n'\beta} u_{ln\alpha} u_{l'n'\beta} \\ &+ \frac{1}{3!} \sum_{ln\alpha} \sum_{l'n'\beta} \sum_{l''n''\gamma} \Phi_{ln\alpha}^{l'n'\beta;l''n''\gamma} u_{ln\alpha} u_{l'n'\beta} u_{l''n''\gamma} + \dots, \end{aligned} \quad (2.15)$$

where E_0 is the potential energy of the crystal in equilibrium and

$$\Phi_{ln\alpha} = \left. \frac{\partial E}{\partial u_{ln\alpha}} \right|_{u=0} = 0, \quad (2.16)$$

$$\Phi_{ln\alpha}^{l'n'\beta} = \left. \frac{\partial^2 E}{\partial u_{ln\alpha} \partial u_{l'n'\beta}} \right|_{u=0}, \quad (2.17)$$

$$\Phi_{ln\alpha}^{l'n'\beta;l''n''\gamma} = \left. \frac{\partial^3 E}{\partial u_{ln\alpha} \partial u_{l'n'\beta} \partial u_{l''n''\gamma}} \right|_{u=0}, \quad (2.18)$$

are the force constants (FCs). These FCs are further labelled as 1FC, 2FC and 3FC depending on the rank of the derivative with respect to the displacements. The 1FC is the negative of the force on atom ln in direction α when all other atoms in the crystal are in their equilibrium positions. Clearly this is zero. The quantity $-\Phi_{ln\alpha}^{l'n'\beta} u_{l'n'\beta}$ describes the force on an atom ln in direction α when an atom $l'n'$ is displaced in direction β , and similarly for the 3FC when the atoms denoted by the superscripts are displaced.

These FCs are important as they are directly related to the properties of phonon modes in the crystal. For example, in the harmonic approximation, determining the 2FC is needed to calculate the frequencies of the phonon modes, which we will later do with DFPT. The knowledge of the 3FC and higher are needed to describe the anharmonic effects, such as the lifetimes of the phonon modes. As these FCs are given by the change of the potential energy with respect to the displacements of atoms in different directions, they also obey the symmetries of the lattice. Therefore, we can also use group theory to discuss the properties of phonons arising from these FCs without evaluating them.

2.2.1 Dynamical matrix in the harmonic approximation

In the harmonic approximation only the 2FC is considered. From the above described relation between the force and the 2FC, a classical equation of motion for the displacement of an atom ln with mass M_l in direction α can be written as,

$$M_l \frac{\partial^2 u_{ln\alpha}}{\partial t^2} + \sum_{l'n'\beta} \Phi_{ln\alpha}^{l'n'\beta} u_{l'n'\beta} = 0. \quad (2.19)$$

This results in $3rN$ differential equations for the r atoms in each of the total N primitive unit cells of the macroscopic crystal which describe the displacements of the atoms.

Fortunately, due to the translational invariance of a crystal, the amount of these differential equations can be reduced. Consider a Fourier ansatz for the displacements with respect to the translation vector, \mathbf{T}_n , and with harmonic time dependence,

$$u_{ln\alpha} = \frac{u_{l\alpha}}{\sqrt{M_l}} e^{i(\mathbf{q}\cdot\mathbf{T}_n - \omega t)}, \quad (2.20)$$

where the mass normalization is conventional. The equation of motion then becomes,

$$\sum_{l'\beta} D'_{l\alpha}{}^{l'\beta}(\mathbf{q}) u_{l'\beta}(\mathbf{q}) = \omega_{\mathbf{q}i}^2 u_{l\alpha}(\mathbf{q}), \quad (2.21)$$

where the dynamical matrix is,

$$D'_{l\alpha}{}^{l'\beta}(\mathbf{q}) = \frac{1}{\sqrt{M_l M_{l'}}} \sum_{n'} \Phi'_{l0\alpha}{}^{l'n'\beta} e^{i\mathbf{q}\cdot(\mathbf{T}_{n'} - \mathbf{T}_0)} = \frac{1}{\sqrt{M_l M_{l'}}} \Phi'_{l\alpha}{}^{l'\beta}(\mathbf{q}). \quad (2.22)$$

The sum in this expression allows for interactions between atoms in the 0th unit cell with atoms in the n th unit cell of the crystal. In practice, the length of this sum depends on the nature of interactions between the atoms. For ionic crystals, where the ions interact via long-range Coulomb forces, many unit cells need to be considered.

For the r atoms in the primitive unit cell, the dynamical matrix results in a $3r \times 3r$ eigenvalue equation for the phonon frequencies $\omega_{\mathbf{q}i}$ and modes $u_{i,l\alpha}$, where the different eigenvalues and modes, corresponding to different phonon branches, have been labelled by index $i = 1, \dots, 3r$. For zincblende InSb with two atoms per primitive unit cell, the dynamical matrix gives six phonon frequencies $\omega_{\mathbf{q}i}$ at every wave vector \mathbf{q} .

For the present thesis, it is important to note two properties of the dynamical matrix. The dynamical matrix can be shown to be Hermitian.^[38] Therefore, its eigenvalues are real and eigenvectors corresponding to non-degenerate eigenvalues are orthogonal, which can be further taken as normalized. The dynamical matrix also satisfies inversion symmetry even if the underlying crystal does not.^[38] Therefore, the phonon frequencies of a branch i at opposite wave vectors are equal, $\omega_{\mathbf{q}i} = \omega_{-\mathbf{q}i}$. This is also a general consequence of the time-reversal symmetry of equations of motions.^[39]

2.2.2 Anharmonic decay of phonons

The harmonic approximation described in the previous section works well for characterizing the phonon frequencies and phonon modes. However, in this approximation the phonons do not interact with each other which leaves out various physical phenomena.^[40] In particular, phonons in perfectly harmonic crystals have infinite lifetimes.

Effects of the phonon-phonon interactions are captured in the frequency dependent anharmonic phonon self-energy,^[41]

$$\Sigma_{\mathbf{q}i}(\omega) = \Delta_{\mathbf{q}i}(\omega) + i\Gamma_{\mathbf{q}i}(\omega), \quad (2.23)$$

where the real part of the self-energy is responsible, for example, to the temperature dependence of the phonon dispersion. The imaginary part of the self-energy is inverse

proportional to the anharmonic lifetime of the phonon,

$$\tau_{\mathbf{q}i}(\omega) = \frac{1}{2\Gamma_{\mathbf{q}i}(\omega)}. \quad (2.24)$$

From a many-body theoretical point of view, the present thesis corresponds to probing the imaginary part of the LO phonon self-energy, which is often discussed in literature.

In the lowest, and also the most dominant order, the anharmonic effects are described by the cubic anharmonic Hamiltonian,

$$H' = \frac{1}{3!} \sum_{ln\alpha} \sum_{l'n'\beta} \sum_{l''n''\gamma} \Phi_{ln\alpha}^{l'n'\beta;l''n''\gamma} u_{ln\alpha} u_{l'n'\beta} u_{l''n''\gamma}, \quad (2.25)$$

where Φ is the 3FC given by the third order derivative of the crystal potential with respect to three atomic displacements, as described in (2.15).

The displacements in (2.25) can be written in terms of the displacement operator,^[38]

$$u_{ln\alpha} = \sqrt{\frac{\hbar}{2NM_l}} \sum_{\mathbf{q}i} \frac{u_{i,l\alpha}(\mathbf{q}) e^{i\mathbf{q}\cdot\mathbf{T}_n}}{\sqrt{\omega_{\mathbf{q}i}}} (b_{\mathbf{q}i} + b_{-\mathbf{q}i}^+), \quad (2.26)$$

where the operators $b_{-\mathbf{q}i}^+$ and $b_{\mathbf{q}i}$ are the boson creation and annihilation operators, which create and annihilate a phonon at momentum and branch $-\mathbf{q}i$ and $\mathbf{q}i$, respectively.

Inserting the displacement operators into (2.25) and abbreviating the phonons by $s = \mathbf{q}i$, the Hamiltonian in second quantization becomes,

$$\hat{H}' = \sum_{ss's''} V_3(s, s', s'') (b_s + b_{-s}^+) (b_{s'} + b_{-s'}^+) (b_{s''} + b_{-s''}^+), \quad (2.27)$$

where $V_3(s, s', s'')$ is the cubic anharmonic potential, which describes the strength of interaction between three phonons, s , s' and s'' . The products of the creation and annihilation operators, $(b_s + b_{-s}^+)$, give rise to 2^3 combinations of possible three phonon interactions. For example, the term $b_s b_{s'} b_{s''}$ describes the simultaneous annihilation of three phonons, while the term $b_{-s}^+ b_{-s'}^+ b_{-s''}^+$ describes simultaneous creation of three phonons. The remaining six terms describe either a decay of one phonon into two other phonons, e.g. a term $b_s b_{-s'}^+ b_{-s''}^+$, or two phonons combining into another phonon, e.g. a term $b_s b_{s'} b_{-s''}^+$.

The cubic anharmonic Hamiltonian can be treated as perturbation on top of the harmonic Hamiltonian with frequencies $\omega_{\mathbf{q}i}$. This gives the general expression for the imaginary part of the anharmonic phonon self-energy via many-body perturbation theory:^[42]

$$\Gamma_s(\omega) = \frac{18\pi}{\hbar^2} \sum_{s's''} |V_3(s, s', s'')|^2 \Delta_{\mathbf{q}\mathbf{q}'\mathbf{q}''} \{ (n_{s'} + n_{s''} + 1) \delta(\omega - \omega_{s'} - \omega_{s''}) \\ + (n_{s'} - n_{s''}) [\delta(\omega + \omega_{s'} - \omega_{s''}) - \delta(\omega - \omega_{s'} + \omega_{s''})] \}. \quad (2.28)$$

Inside the curly brackets, the mean thermal occupation number of a phonon is given by the Bose-Einstein distribution, $n_s = 1/[\exp(\hbar\omega_s/k_B T) - 1]$, and the delta functions $\delta(\dots)$ ensure energy conservation in the decays. The first term describes a process where an excited phonon s decays into two other phonons s' and s'' . The second term describes a

process where the excited phonon combines with a thermal phonon resulting in a third higher energy phonon, either s' or s'' . For the near zone center LO phonon, which is the highest frequency mode due to the LO-TO splitting in polar semiconductors, the second process is not allowed by energy conservation.

The function $\Delta_{\mathbf{q}\mathbf{q}'\mathbf{q}''}$ in (2.28) is equal to one if $\mathbf{q} + \mathbf{q}' + \mathbf{q}'' = \mathbf{G}_{hkl}$ and zero otherwise. Considering only normal processes, $\mathbf{G}_{hkl} = 0$, and imposing this momentum conservation, the cubic anharmonic potential for a zone center phonon is,

$$\begin{aligned}
V_3(\mathbf{0}i, \mathbf{q}'i', -\mathbf{q}''i'') &= \frac{1}{3!} \left(\frac{\hbar^3}{8N^3 \omega_{\mathbf{0}i} \omega_{\mathbf{q}'i'} \omega_{-\mathbf{q}''i''}} \right)^{1/2} \\
&\times \sum_{l'l''} \sum_{\alpha\beta\gamma} \sum_{n'n''} \Phi_{ln\alpha}^{l'n'\beta; l''n''\gamma} e^{i\mathbf{q}' \cdot (\mathbf{T}_{n'} - \mathbf{T}_{n''})} \\
&\times \frac{u_{i,l\alpha}(\mathbf{0}) u_{i',l'\beta}(\mathbf{q}') u_{i'',l''\gamma}(-\mathbf{q}')}{\sqrt{M_l M_{l'} M_{l''}}}.
\end{aligned} \tag{2.29}$$

The lifetime of a phonon s is given as the sum over all the decay channels s' and s'' that conserve energy and crystal momentum. Apart from the mean occupation numbers, n_s , the coupling rate of a phonon s to phonons s' and s'' is determined by these potentials. Debernardi^[11, 43] has studied the analytical limit of the 3FC and the eigenvectors in this potential. He has shown that in the long wavelength limit, the coupling rate of a zone center optical phonon with two acoustic phonons scales quadratically with magnitude of the wave vector of the acoustic phonons and linearly for the coupling with one optic and one acoustic phonon. This implies that the anharmonic decay of a zone center optical phonon does not favor small wave vector phonons, and these channels should have small contributions to its anharmonic lifetime. Furthermore, we note that, if the rate is taken as: $\Gamma_{\text{LO}}(\omega_{\text{LO}}) \sim (n_{s'} + n_{s''} + 1)/(\omega_{\text{LO}}\omega_{s'}\omega_{s''})$, it is larger for two non-degenerate phonons over two degenerate phonons, which together conserve the LO phonon energy.

2.2.3 Group theory of phonons in zincblende

Group theory is a powerful tool for determining properties of solids entirely based on the symmetry of the crystal structure. In particular, this gives us the means to understand the phonon dispersion in solids, as the modes and their degeneracies are given by the irreducible representations (irreps) they transform as. Furthermore, if the modes are characterised in terms of their irreps, the selection rules for the THz excitation can be determined. We will discuss these concepts for the phonons at the Γ point of zincblende.

It is worth to mention that group theory consists of various abstract concepts which are difficult to introduce in any formality, while keeping the discussion applied to the present thesis. Therefore, for a reader unfamiliar with basics of group theory, further information can be gained by consulting the excellent books by Dresselhaus et al.^[44] or chapter 5 by Atkins.^[45] The theoretical formulation described here follows closely to the lecture notes by F. Aryasetiawan for a course on group theory at Lund University.^[46] Similar theoretical treatment can be also found given by Elliot and Dawber.^[47]

The space group of the zincblende InSb in different notations is $(T_d^2, F\bar{4}3m, \#216)$. This group consists of a group formed by the lattice translation vectors, $\{\mathbf{T}_n\}$, and the

point group of a tetrahedron T_d . This tetrahedral point group consists of 24 symmetry operations in six different classes, which can be found described in appendix B. In representation theory, these symmetry operations are represented by square matrices in a basis chosen for the representation (rep). This chosen rep is entirely characterized by the traces of the matrices belonging to the different classes of the group.

Rep, χ^{rep} , can be decomposed into a direct sum of the irreps, χ^α , of the group,

$$\chi^{\text{rep}} = \sum_{\alpha} m_{\alpha} \chi^{\alpha}, \quad (2.30)$$

where the multiplicity m_{α} describes how many times an irrep α occurs in the decomposition. This multiplicity is given by,

$$m_{\alpha} = \frac{1}{h} \sum_k N_k \chi^{\alpha*}(C_k) \chi^{\text{rep}}(C_k), \quad (2.31)$$

where h is the number of elements in the group and the sum is over the classes C_k of the group each containing N_k elements. $\chi^{\alpha}(C_k)$ are the characters of the irreps of the classes of the group, which can be found in various sources.^[44,48] For convenience, we have also tabulated the characters of the irreps for the T_d group in table 5 in appendix B.

The relevant rep for discussing phonons in zincblende InSb is the six-dimensional direct product rep of the Cartesian basis and the two basis atoms in the primitive unit cell. In appendix B, we have identified that the characters of the classes of the T_d group in this basis are: $\chi^{\text{InSb}}(C_k) = \chi^{\text{atoms}}(C_k) \chi^{xyz}(C_k) = 2(3, 0, -1, -1, 1)$, where $\chi^{\text{atoms}}(C_k) = 2$ for all classes of the group due to the group of translations. Using (2.30) and the character table 5 in the appendix B, this decomposes into $\chi^{\text{InSb}} = 2T_2$. From the character table, we can further identify that, $\chi^{xyz} = \chi^{T_2}$, and the Cartesian axes (x, y, z) transform as the irrep T_2 . In appendix B, we also show that this is the case for their products (xy, yz, xz) .

To discuss phonons, or other properties of solids, in terms of group theory it is necessary to consider the wave vectors groups of the high-symmetry points in the IBZ. Due to the Wigner-Seitz cell construction of the BZ, the wave vector group of the Γ point is given by the entire point group of the real space lattice. (The other high-symmetry points are subgroups of this group.) Therefore, the decomposition at the Γ point is also $\chi^{\text{InSb}} = 2T_2$, where T_2 in the notation by Koster is the Γ_{15} irrep.^[49]

If an operator is written in the symmetry adapted basis transforming as the irreps in the decomposition, it will be partially diagonalized in a block diagonal form.^[47] In particular for the decomposition $2T_2$, the dynamical matrix at the Γ point will consist of three degenerate blocks. This degeneracy is due to the fact that the irrep T_2 is three-dimensional and, therefore, it has three degenerate basis functions. Each of these three blocks will be of dimension (2×2) , which give two non-degenerate eigenvalues and modes for the phonons at the Γ point of InSb. This is a consequence of the multiplicity $m_{T_2} = 2$ in the decomposition, which means that there is two distinct sets of the three-fold degenerate basis functions. Together, the three (2×2) blocks match the dimension of the dynamical matrix, which for a crystal containing two atoms per primitive unit cell is (6×6) .

In general, the symmetry adapted basis can be constructed from arbitrary functions by applying the projection operator.^[47] However, for the dynamical matrix, we have

identified that the three-dimensional basis of T_2 is (x, y, z) . Thus, we can directly write that the set of functions which give the three degenerate, two-dimensional blocks are the Cartesian axes on each of the two In and Sb atom: $(x_{\text{In}}, x_{\text{Sb}})$, $(y_{\text{In}}, y_{\text{Sb}})$ and $(z_{\text{In}}, z_{\text{Sb}})$.

The vibrational modes are given by linear combinations of these distinct functions.^[47] The two distinct orthonormal eigenvectors of the Hermitian dynamical matrix at the Γ point are, $2^{-1/2}(x_{\text{In}} \pm x_{\text{Sb}})$, and similarly for the y - and z -directions, where the plus sign corresponds to an acoustic mode and the minus sign corresponds to an optic mode. For the acoustic modes, the atoms in the primitive unit cell, and at the exact zone center in the entire lattice, move exactly in phase. For the optic modes, the displacements of the atoms are out of phase. From a vibrational mode point of view, the acoustic modes exactly at the zone center correspond to translating the entire crystal. Therefore, the acoustic frequencies at the Γ point are zero. From this we can define that all the phonon branches with zero frequency at $\mathbf{q} = 0$ are acoustic and the remaining branches are optic. We note that at non-zero wave vectors, the displacement of an atom l in direction α in the unit cell n of the macroscopic crystal dephases with respect to the same atom in the 0th unit cell, $u_{i,l n \alpha} = u_{i,l 0 \alpha} \exp(i\mathbf{q} \cdot \mathbf{T}_n)$, as already given in (2.20). Therefore, the acoustic modes at non-zero wave vectors will also have non-zero frequencies.

We have determined above that both the acoustic and optic modes at the Γ point of zincblende are three-fold degenerate due to the Cartesian directions being degenerate. We further note that a basic theorem in linear algebra proves that a linear combination of eigenvectors with degenerate eigenvalues, is also an eigenvector with the same eigenvalue¹. Therefore, due to the large degeneracy of the Γ point, the two distinct set of modes, acoustic and optic, can consists of linear combinations of the Cartesian directions.

After having classified that the optic phonon modes at the Γ point of zincblende InSb transform as T_2 , we can characterize their selection rules for the THz excitation. Transition rate from an initial state i to final states f due to weak perturbation H' can be described by the Fermi's golden rule,^[50]

$$\Gamma_{i \rightarrow f} = \frac{2\pi}{\hbar} \sum_f |\langle f | \hat{H}' | i \rangle|^2 \delta(E_f - E_i). \quad (2.32)$$

Transition can be defined as forbidden if the rate is strictly zero. This is true if the matrix element $\langle f | \hat{H}' | i \rangle$ in the above is zero.

The task of determining whether a matrix element is zero can be greatly reduced if the states and operators are characterized in terms of their irreps, $\alpha\beta\gamma$. In this form, a general matrix element, such as the above, can be written as,

$$(\psi^\gamma, \hat{O}^\beta \psi^\alpha) \equiv \int d^3r \psi^{\gamma*}(\mathbf{r}) \hat{O}^\beta \psi^\alpha(\mathbf{r}). \quad (2.33)$$

This matrix element is not necessarily zero, if the direct product rep of the irreps α and β contains the irrep γ ,

$$T^\alpha \otimes T^\beta \subseteq T^\gamma, \quad (2.34)$$

where T^i denotes the matrix rep of the irrep i . This condition can be proven from the properties of the Clebsch–Gordan coefficients arising from writing the matrix element in

¹This can be proved in one line by considering: $A\mathbf{u} = A \sum_i c_i u_i = \lambda \sum_i c_i u_i = \lambda \mathbf{u}$ where $Au_i = \lambda u_i$.

terms of the Wigner-Eckart theorem.^[38,47] The discussed partial diagonalization of the dynamical matrix in the symmetry adapted basis also follows from this theorem.

Determining whether (2.34) holds can be done from the characters of the irreps. As the character of a rep is defined to be given by the trace, which is independent of the basis. The character of a direct product rep is simply the product of the traces of the reps, i.e., $\text{Tr}(T^\alpha \otimes T^\beta) = \chi^\alpha \chi^\beta$. Therefore, the condition in (2.34) can also be stated as: If in the decomposition of the characters of the direct product rep,

$$\chi^\alpha \chi^\beta = \sum_{\gamma} m_{\alpha\beta\gamma} \chi^\gamma, \quad (2.35)$$

the multiplicity of the irrep γ ,

$$m_{\alpha\beta\gamma} = \frac{1}{h} \sum_k N_k \chi^\alpha(C_k) \chi^\beta(C_k) \chi^{\gamma*}(C_k), \quad (2.36)$$

is non-zero, then the matrix element $(\psi^\gamma, \hat{O}^\beta \psi^\alpha)$ is not necessarily zero. It is not difficult to determine this, as calculating the multiplicity amounts to summing over the products of the characters of the classes in the rows labelled by $\alpha\beta\gamma$ in the character table.

With the above theoretical formulation, we can determine the selection rules for the optical activity of the T_2 phonon mode at the Γ point of zincblende InSb. The dipole operators are described by $\hat{H}' \propto \{\hat{x}, \hat{y}, \hat{z}\}$, which transform as the Cartesian directions and, therefore, also as the irrep T_2 . The T_2 phonon mode can be excited by dipole radiation, if the initial state transforming as the irrep α satisfies the condition given by (2.34): $T^\alpha \otimes T^{T_2} \subseteq T^{T_2}$. If the initial state is taken as the ground state, which can be assumed to transform as the totally symmetric identity rep A_1 of the group. This gives the multiplicity from (2.36) as $m_{A_1, T_2, T_2} = 1$. Therefore, the T_2 phonon mode is dipole active for all polarizations. We have also determined that the quadrupole operators described by $\hat{H}' \propto \{\hat{x}\hat{y}, \hat{y}\hat{z}, \hat{x}\hat{z}\}$ transform as the irrep T_2 and the same argument holds as well. Thus, the T_2 phonon mode is also Raman active.

3 Theoretical Methods

In this section we will describe the theoretical methods used to model the TXRD intensity of the weak reflections due to the THz excited LO phonons. First, we will characterize the force term of the harmonic oscillator equations used to model the displacements of the atoms in the THz excited LO phonons. We will also discuss both the analytical and numerical solution of these equations, depending whether the temporal profiles of the THz electric fields in the force term are modelled by Dirac delta or Gaussian distributions.

The material parameters needed for the harmonic oscillator model are simulated with DFPT, which builds upon the ground state simulated by density functional theory (DFT). Therefore, in this section we will first describe the aspects of DFT to guarantee that we can correctly produce the ground state of InSb. After this, we will describe the DFPT equations to be solved for the harmonic oscillator model.

3.1 Harmonic oscillator model for the THz excited phonons

Force on an atom A in a Cartesian direction i due to external field components E_i can be described by (with implicit summation over the repeated indices),

$$F_{A,i} = Z_{A,ij}^* E_j + \varepsilon_0 \Omega_0 \frac{\partial \chi_{jk}^{(1)}}{\partial r_{A,i}} E_j E_k, \quad (3.1)$$

where $Z_{A,ij}$ is the Born effective charge of an ion A in the crystal due to ionic bonding. In general, this Born effective charge is a second rank tensor i.e., (3×3) matrix in Cartesian basis. However, in cubic materials the Cartesian directions are degenerate and this tensor is diagonal where all the elements are equal,

$$\mathbf{Z}_A^* = \begin{bmatrix} Z_{A,xx}^* & & \\ & Z_{A,yy}^* & \\ & & Z_{A,zz}^* \end{bmatrix} = Z_A^* \mathbf{I}, \quad (3.2)$$

where \mathbf{I} is an identity matrix. Interpretation of the structure of this tensor is that an applied field in a Cartesian direction will result in a force in the same direction.

Derivative of the jk component of the linear susceptibility $\chi_{jk}^{(1)}$ with respect to a displacement of an atom A from its equilibrium position $r_{A,i}$ is the Raman tensor. This Raman tensor is a third rank tensor, which can be constructed from the the quadrupole electric field operators that can excite the phonon mode from the ground state.^[51] As shown in the group theory section, the T_2 phonon mode is Raman active for the quadrupole operators (xy, yz, xz) . Therefore, the Raman tensor has the following structure,

$$\begin{aligned} \frac{\partial \chi_{A,jk}^{(1)}}{\partial r_{A,i}} &= \left\{ \frac{\partial \chi_{A,jk}^{(1)}}{\partial r_{A,x}}, \frac{\partial \chi_{A,jk}^{(1)}}{\partial r_{A,y}}, \frac{\partial \chi_{A,jk}^{(1)}}{\partial r_{A,z}} \right\} \\ &= \left\{ \begin{bmatrix} & & \\ & d_{A,yz} & \\ d_{A,zy} & & \end{bmatrix}, \begin{bmatrix} & d_{A,xz} & \\ & & \\ d_{A,zx} & & \end{bmatrix}, \begin{bmatrix} & d_{A,xy} & \\ & & \\ d_{A,yx} & & \end{bmatrix} \right\}, \end{aligned} \quad (3.3)$$

where all the non-zero elements $d_{A,jk}$ are equal. The structure of the Raman tensor is such that for fields E_y and E_z the force on an atom A is in the x -direction and so on.

Forces on the In atoms due to the external fields can then be written as,

$$\begin{aligned} F_{\text{In},x} &= Z_{\text{In}}^* E_x + 2\varepsilon_0 \Omega_0 d_{\text{In}} E_y E_z, \\ F_{\text{In},y} &= Z_{\text{In}}^* E_y + 2\varepsilon_0 \Omega_0 d_{\text{In}} E_x E_z, \\ F_{\text{In},z} &= Z_{\text{In}}^* E_z + 2\varepsilon_0 \Omega_0 d_{\text{In}} E_x E_y, \end{aligned} \quad (3.4)$$

where the fields have time dependence, but we will neglect the spatial dependence due to absorption by assuming that the THz pulse excites the x-ray probe volume evenly.

For materials with ionic bonding, one can predict that the forces due to the terms linear in the fields will dominate. However, if the fields are strong enough, the terms quadratic in the fields can become significant and we will keep them for generality. Furthermore, the forces due to the Raman terms also apply for optical phonon excitation in diamond structures, which are non-polar by the fact that their effective charges are zero.

For the above forces, we can model the phonon dynamics due to the THz excitation by a set of driven damped harmonic oscillators, as already given in the introduction,

$$\left(\frac{\partial^2}{\partial t^2} + 2\Gamma\frac{\partial}{\partial t} + \omega_0^2\right)u_{\text{In},i} = \frac{F_{\text{In},i}}{M_{\text{In}}}, \quad (3.5)$$

where $u_{\text{In},i}$ is the displacement of an In atom with mass M_{In} from its equilibrium position in direction i . The damping parameter is inverse of the anharmonic lifetime, $2\Gamma = 1/\tau$, of the phonon mode with frequency ω_0 . Similar set can be constructed for the Sb atoms.

If the material parameters were known, the solutions $u_{A,i}$, for chosen fields of the THz radiation can be inserted into the structure factor (1.2) to evaluate the TXRD intensity. We will determine the material parameters, apart from the damping, using DFPT. However, the electric fields for the THz radiation will still need to be modelled. It is worthwhile to discuss solving these inhomogenous differential equations for different temporal profiles of the electric fields.

In the simplest case, the electric fields of an ultrashort laser pulse can be taken to have temporal profiles described by a Dirac delta function, $\mathbf{E}(t) = \mathbf{E}_0\delta(t) = [E_{0x}, E_{0y}, E_{0z}]\delta(t)$. For these fields, the driven damped harmonic oscillators can be solved via the Green's function technique,^[52] which gives the displacements of the In atoms as,

$$u_{\text{In},i} = A_{0,i}e^{-\Gamma t} \sin(\sqrt{\omega_0^2 - \Gamma^2}t). \quad (3.6)$$

The displacements have sinusoidal time dependence with resonance frequency $\omega^2 = \omega_0^2 - \Gamma^2$ and they decay exponentially with the damping Γ . All the information on the electric fields is contained in the constant $A_{0,i}$, which is determined by the initial amplitude of oscillation due to the excitation. Typically $\Gamma \ll \omega_0$ and the square of the damping Γ in the argument of the sine function can be neglected. Therefore, this analytical solution is useful as it offers a model to fit the damping parameter from exponential decay of the oscillation amplitude after an excitation. This is the method choice in literature to extract the damping parameter from experimental data,^[53–55] as characterizing the force requires state of the art electronic structure theory and precise knowledge of the excitation.

The above analytical solution for the fields with delta function temporal profile yields no prior information about the oscillation amplitudes and the required field parameters. Therefore, to model the TXRD intensity due to the THz excitation, it is better and more accurate to describe the field to have a Gaussian envelope,

$$\mathbf{E}(t) = [E_{0x}, E_{0y}, E_{0z}]e^{-(t/\tau_G)^2} e^{i\omega_{\text{THz}}t}, \quad (3.7)$$

where ω_{THz} is the carrier frequency of the ultrashort pulse and τ_G is related to the FWHM of the intensity of the pulse as, $\tau_{\text{FWHM}} = \sqrt{2 \ln 2} \tau_G$. The spectral intensity of this pulse is also a Gaussian, $S(\omega) \propto \exp(-[\tau_G(\omega - \omega_{\text{THz}})]^2/2)$, and its spectral FWHM is given by the time-bandwidth product, $\omega_{\text{FWHM}} = 2\pi \times 0.44/\tau_{\text{FWHM}}$.^[56]

Since the Raman terms in the force are quadratic in the fields, the Raman excitation based on this harmonic oscillator model will resonate for THz carrier frequency at half the phonon frequency, $\omega_{\text{THz}} = \omega_0/2$. This is a two photon process, known as the sum-frequency Raman excitation, which has recently been demonstrated as the method to excite coherent optical phonons in diamond with large oscillation amplitudes.^[53,57]

It is possible to solve the harmonic oscillator equations via the Green's function technique analytically even for these Gaussian fields. However, this gives the displacements as lengthy linear combinations of real and complex error functions, which would then need to be integrated numerically or approximated from their Taylor expansions. This method introduces errors, especially for small times. Therefore, it is better to solve the harmonic oscillators equations for the Gaussian fields numerically.

For numerically solving differential equations with various different time scales; the rapid phonon oscillation and its slow decay, carrier frequency of the pulse and its Gaussian envelope, special care must be taken as this can become numerically unstable for non-stiff methods. Therefore, for solving the harmonic oscillators we have relied on the LSODA algorithm^[58] with automatic stiffness detection, as implemented in the scientific Python package.^[59] The Python scripts used in this thesis are further documented on GitHub.^[60]

3.2 Density functional theory

In the adiabatic approximation by Born and Oppenheimer,^[61] the potential energy E of a crystal for fixed positions of nuclei is given by the N -electron Schrödinger equation,

$$\hat{H}\Psi(\mathbf{r}_1, \mathbf{r}_2, \dots, \mathbf{r}_N) = E\Psi(\mathbf{r}_1, \mathbf{r}_2, \dots, \mathbf{r}_N), \quad (3.8)$$

where the Hamiltonian, (in Hartree units: $e = \hbar = m_e = 4\pi\epsilon_0 = 1$), is,

$$\hat{H} = -\frac{1}{2} \sum_i^N \nabla_i^2 + \sum_i^N v_{\text{ext}}(\mathbf{r}_i) + \frac{1}{2} \sum_{i \neq j}^N \frac{1}{|\mathbf{r}_i - \mathbf{r}_j|} + E_{\text{NN}}. \quad (3.9)$$

The first term is the kinetic energy operator \hat{T} and the second term is the external potential \hat{V}_{ext} , describing the interaction between the electrons and the fixed nuclei. The third term, that depends on the positions of two electrons, \mathbf{r}_i and \mathbf{r}_j , is the electron-electron interaction term, \hat{V}_{ee} and the last term is the electrostatic energy between nuclei.

Due to the two particle dependency of the electron-electron term, the Hamiltonian cannot be decoupled into one-particle Hamiltonians which could be solved. While this term makes the solutions of the many-body Schrödinger equation impossible, it is also the term that is needed for accurately describing various properties in the condensed matter.

In the present thesis, DFT is the method of choice for solving the crystal potential from the above many-body problem, which is needed, for example, to determine the FCs to simulate the phonons with DFPT. In these theories, the effects of the exchange and correlation (XC) arising from the quantum mechanical electron-electron interaction are approximated from a homogeneous electron gas. This electron gas approximation often works well, however, it is well known to severely underestimate the electronic band gaps of insulators.^[62] This introduces an obstacle for the present thesis, as we are interested in characterizing electric field responses of polar optical phonons in the small band gap InSb. Therefore, in this section we will review the theory of DFT to the extent that we can form a method to guarantee that InSb is correctly described as a semiconductor with our choices of the XC functional and pseudopotentials. We will further describe the practical aspects of these simulations for periodic solids, such as the k -point sampling

and the plane wave basis, which result in convergence parameters that are important for achieving high quality simulations both at the DFT and DFPT level.

3.2.1 Self-consistent Kohn-Sham equations

The theoretical framework of DFT is based on the theorems by Hohenberg and Kohn.^[63] These theorems prove that the external potential is uniquely determined by the electron density, and that there exists an universal density functional in terms of which the total energy can be described. The density that minimizes this total energy is the true ground state density corresponding to the true ground state total energy.

While these theorems circumvent the otherwise impossible task of characterizing the many-body wave function by introducing the density. Hohenberg and Kohn did not manage to give an accurate description for the universal density functional. In particular, it has been difficult to formulate the many-body kinetic energy as a functional of density.

Kohn and Sham (KS) replaced the problem of finding the ground state density of the interacting system with an auxiliary non-interacting system, under the assumption that the ground state densities of the non-interacting and the interacting systems are equal.^[64] The genius of this proposal was that the kinetic energy could now be determined from the one-particle orbitals $\phi_i(\mathbf{r})$ of the non-interacting system,

$$T_0[\rho] = - \sum_i^{N/2} \int d^3r \phi_i^*(\mathbf{r}) \nabla^2 \phi_i(\mathbf{r}), \quad (3.10)$$

where it has been assumed that the system is non-magnetic such that each of the lowest occupied $N/2$ orbitals is occupied twice.

In terms of this non-interacting kinetic energy, the KS total energy of the interacting many-body system is,

$$E_{\text{KS}}[\rho] = T_0[\rho] + E_{\text{H}}[\rho] + E_{\text{XC}}^{\text{DFT}}[\rho] + \int d^3r v_{\text{ext}}(\mathbf{r})\rho(\mathbf{r}), \quad (3.11)$$

where the Hartree term describes the Coulomb interaction between two charge densities,

$$E_{\text{H}}[\rho] = \frac{1}{2} \sum_{ij}^{\text{occ}} \int d^3r d^3r' \frac{\phi_i(\mathbf{r})\phi_i^*(\mathbf{r})\phi_j(\mathbf{r}')\phi_j^*(\mathbf{r}')}{|\mathbf{r} - \mathbf{r}'|} = \frac{1}{2} \int d^3r d^3r' \frac{\rho(\mathbf{r})\rho(\mathbf{r}')}{|\mathbf{r} - \mathbf{r}'|}. \quad (3.12)$$

It is necessary to sum over the self-interaction term, $i = j$, to write E_{H} in terms of the two densities. The term $E_{\text{XC}}^{\text{DFT}}[\rho]$ in (3.11) is the XC functional of DFT, which should also account for the fact that kinetic energy is evaluated in the non-interacting KS system.

The density which minimizes the KS total energy is also evaluated from the (doubly occupied) one-particle orbitals of the non-interacting system,

$$\rho(\mathbf{r}) = 2 \sum_i^{N/2} |\phi_i(\mathbf{r})|^2. \quad (3.13)$$

These orbitals are given by solving the KS equations,

$$\left[-\frac{1}{2}\nabla^2 + V_{\text{KS}}(\mathbf{r}) \right] \phi_i(\mathbf{r}) = \varepsilon_i \phi_i(\mathbf{r}), \quad (3.14)$$

where the electron in the non-interacting system feels the effective KS potential,

$$V_{\text{KS}}(\mathbf{r}) = \int d^3r' \frac{\rho(\mathbf{r}')}{|\mathbf{r} - \mathbf{r}'|} + \frac{\delta E_{\text{XC}}^{\text{DFT}}[\rho]}{\delta \rho(\mathbf{r})} + v_{\text{ext}}(\mathbf{r}). \quad (3.15)$$

These equations are then solved self-consistently. Starting from an initial guess of the density, KS potential can be constructed. Solutions of the KS equations then give a new density, which can be used to calculate the KS total energy and related properties of the interacting many-body system. For this new density, a new KS potential can be constructed and the KS equations can again be solved for a new density. This is repeated until the change in a parameter, such as the total energy, between two concurrent loops is smaller than an user defined convergence parameter.

3.2.2 Exchange and correlation functional

To solve the KS scheme, parametrization for the XC functional is needed and in DFT this is approximated from the homogeneous electron gas. However, before discussing these approximate functionals, we will review the XC in general to understand its effect and the underlying approximations made in DFT. In particular, we will highlight the role of the exchange interaction to the self-interaction error (SIE) present in the Hartree term.

The exchange interaction arises strictly from the antisymmetry of the fermionic wave function under the exchange of two identical fermions, as demanded by the Pauli principle. This antisymmetry requirement can be met by describing the many-body wave function in terms of Slater determinants. If the wave function is approximated by a single Slater determinant, also known as the Hartree-Fock approximation (HFA), the difference between the many-body electron-electron interaction in a single Slater determinant basis and the classical Hartree interaction is defined to give the exact exchange. The total exchange energy can then be expressed in terms of the occupied atomic orbitals $\{\phi\}$ as,

$$E_{\text{X}}[\{\phi\}] = \langle \hat{V}_{\text{ee}} \rangle_{\text{HFA}} - E_{\text{H}}[\rho] = -\frac{1}{2} \sum_{ij}^{\text{occ}} \int d^3r d^3r' \frac{\phi_i(\mathbf{r})\phi_i^*(\mathbf{r}')\phi_j^*(\mathbf{r})\phi_j(\mathbf{r}')}{|\mathbf{r} - \mathbf{r}'|} \delta_{\sigma\sigma'}, \quad (3.16)$$

where the summation also contains the spin variable σ and we have highlighted by the Kronecker delta, $\delta_{\sigma\sigma'}$, that the exchange interaction is a pair interaction between electrons of the same spin only. However, if only one electron, $i = j$, is considered, the exchange gives $E_{\text{X}} = -E_{\text{H}}$ and thus $\langle \hat{V}_{\text{ee}} \rangle_{\text{HFA}} = 0$. This is important as the exact orbital dependent exchange interaction cancels the self-interaction of the electron with itself in the Hartree term and which would otherwise cause the one-particle energies to be too large.

In general, the many-body wave function should be written as an infinite linear combination of the Slater determinants (configurations). The correlation energy can then be conceptually defined as the difference between the HFA and the exact electron-electron interaction, $\langle \hat{V}_{\text{ee}} \rangle - \langle \hat{V}_{\text{ee}} \rangle_{\text{HFA}}$. However, unlike the exchange, it is practically impossible to calculate this and approximations are needed.

In the local density approximation (LDA) of DFT, the XC are both approximated from the homogeneous electron gas, where all the electrons are separated by $R = |\mathbf{r} - \mathbf{r}'|$. As shown in appendix D, the exchange part can be straightforwardly calculated by inserting

plane waves, $\phi_i(\mathbf{r}) = \exp(i\mathbf{k}_i \cdot \mathbf{r})/\sqrt{V}$, where V is volume of the gas, into (3.16). This gives the exchange energy per particle per spin in a non-magnetic electron gas as,

$$\varepsilon_X[\rho(\mathbf{r})] = \frac{E_X}{N} = -\frac{3}{4\pi}(3\pi^2\rho(\mathbf{r}))^{1/3}, \quad (3.17)$$

where N is the number of electrons per spin in the gas. The exchange interaction is thus an average quantity that depends on the density of the gas via the density given by the KS orbitals and the explicit dependence on the underlying atomic orbitals is lost.

The correlation cannot be calculated analytically even for the homogeneous electron gas. However, as also shown in appendix D, it is possible to express the total XC in terms of a pair distribution function. For the homogeneous gas, this function describes the probability that two electrons are separated by a distance R in the gas. Based on this approach, the correlation can be parametrized as a functional of the electron gas density using the Quantum Monte Carlo simulation data of the homogeneous electron gas by Ceperley and Alder.^[65] Various parametrizations exist in literature and for the present thesis we note, in particular, the parametrization by Perdew and Wang.^[66]

The total XC in the LDA of DFT is then integrated point-wise using the result from the homogeneous electron gas, $\varepsilon_{XC} = \varepsilon_X + \varepsilon_C$, over a system which is not homogeneous,

$$E_{XC}^{\text{LDA}}[\rho] = \int d^3r \rho(\mathbf{r}) \varepsilon_{XC}[\rho(\mathbf{r})]. \quad (3.18)$$

In addition to the LDA, common class of XC functionals are the functionals in the generalized gradient approximation (GGA). These functionals have attempted to include the effects of the in-homogeneity of real systems by also considering gradients of the density in the expression for the XC.^[67] However, while these gradient considerations have been shown to better describe finite systems, such as molecules or surfaces, they are not an improvement for infinite systems such as bulk solids.^[68] In particular, for the present thesis, He et al.^[69] have studied that LDA outperforms GGA for describing the vibrational properties of solids. However, they both fail to describe dielectric properties due to the severe underestimation of the band gap. More advanced functionals exist that can resolve this band gap problem.^[70–73] However, it is more difficult to implement these also on the DFPT level and we do not consider them here. We will address this band gap problem later by the choice of pseudopotentials at the LDA level of DFT.

3.2.3 Plane waves and pseudopotentials

To solve the KS equations a basis set has to be chosen and for periodic solids a common choice are plane waves. This plane wave basis gives rise to a convergence parameter and it is also used in conjunction with pseudopotentials as will be discussed here.

In a periodic solid, the wave functions are known to take the form of Bloch waves,^[40]

$$\phi_{i\mathbf{k}}(\mathbf{r}) = u_i(\mathbf{r})e^{i\mathbf{k}\cdot\mathbf{r}}, \quad (3.19)$$

where i labels band index and the wave vector \mathbf{k} is restricted to the first BZ. The cell periodic part, $u_i(\mathbf{r}) = u_i(\mathbf{r} + \mathbf{T}_n)$, can be written as a Fourier series,

$$u_i(\mathbf{r}) = \sum_{\mathbf{G}} c_{i,\mathbf{G}} e^{i\mathbf{G}\cdot\mathbf{r}}, \quad (3.20)$$

where \mathbf{G} is a reciprocal lattice vector. This gives (3.19) as a sum of plane waves,

$$\phi_{i\mathbf{k}}(\mathbf{r}) = \sum_{\mathbf{G}} c_{i,\mathbf{k}+\mathbf{G}} e^{i(\mathbf{k}+\mathbf{G})\cdot\mathbf{r}}. \quad (3.21)$$

Using this plane wave expansion, the KS equation (3.14) becomes an eigenvalue equation,

$$\sum_{\mathbf{G}'} \left[\frac{1}{2} |\mathbf{k} + \mathbf{G}'|^2 \delta_{\mathbf{G}\mathbf{G}'} + V_{\text{KS}}(\mathbf{G} - \mathbf{G}') \right] c_{i,\mathbf{k}+\mathbf{G}'} = \varepsilon_{i\mathbf{k}} c_{i,\mathbf{k}+\mathbf{G}}. \quad (3.22)$$

The dimension of the eigenvalue problem to be solved is given by the number of Fourier coefficients $c_{i,\mathbf{k}+\mathbf{G}}$ in the plane wave expansion. This number is often characterized by the value of kinetic energy of the corresponding plane wave, also known as the plane wave cut-off energy: $E_{\text{cut}} \leq \frac{1}{2} |\mathbf{k} + \mathbf{G}|^2$ in Hartree units. In general, an infinite set of plane waves would be needed to accurately describe a periodic function. However, the plane waves with large kinetic energy are often less important and the expansion can be truncated by only considering plane waves below an user defined cut-off energy. While this truncation reduces the simulation time, the cut-off energy is an important convergence parameter in plane wave DFT. In particular, it is always necessary to study that the parameter of interest is converged with respect to the number of plane waves used in the basis set.

As discussed, the plane waves form a complete set of orthonormal functions and any periodic function can be expanded in terms of plane waves. However, the valence orbitals of atoms are highly oscillatory in the core region and an accurate plane wave expansion of an oscillatory function requires many Fourier components. As the number of Fourier components directly gives the dimension of the KS eigenvalue equation to be solved, this becomes computationally unfeasible. Therefore, the goal of introducing pseudopotentials is to remove certain number of core electrons by introducing a cut-off radius and replace the potential below this radius by an effective potential. This allows one to replace the highly oscillatory valence wave functions by smooth pseudo wave functions in the core region, which can then be expanded in a feasible number of plane waves. Above the core region, the pseudopotential and the wave function match their all electron counterparts. These pseudopotentials for DFT are constructed for the periodic table of elements for the chosen XC functional from their all electron potentials. For this construction to be accurate various properties have to be conserved, which is discussed more in Refs. ^[67, 74]

3.2.4 Brillouin zone sampling

From the Bloch theorem it follows that the wave functions and their energies are characterized by the band index i and the wave vectors \mathbf{k} in the first BZ. Various properties, such as calculating the density given by the KS orbitals, require a summation over this band index and an integration with respect to the k -points in the BZ. This integration can be discretized to a finite number of special k -points in the IBZ for efficient numerical simulations and this results in an important convergence parameter as discussed here.

Macroscopic crystal consisting of $N = N_1 N_2 N_3$ unit cells can be taken to satisfy the periodic Born-Von Karman boundary conditions, $\phi_i(\mathbf{r} + N_i \mathbf{a}_i) = \phi_i(\mathbf{r})$, where N_i is the

number of unit cells in the direction of the primitive lattice vector \mathbf{a}_i . The number of k -points in the primitive unit cell of the reciprocal space of this crystal is then given by,^[40]

$$\mathbf{k}_{n_1, n_2, n_3} = \sum_i^3 \frac{n_i}{N_i} \mathbf{b}_i, \quad (3.23)$$

where $n_i = 1, 2, \dots, N_i$ and \mathbf{b}_i is the primitive reciprocal lattice vector. There are exactly as many k -points in the BZ as there are unit cells in the macroscopic crystal, which in practice is infinite. Therefore, the wave vector \mathbf{k} can be treated as continuous. However, the values at k -points close to each other are almost identical and it is possible to choose a smaller set of special k -points for which the BZ is sampled. A commonly used set of such points has been described by Monkhorst and Pack,^[75]

$$\mathbf{k}_{n_1, n_2, n_3} = \sum_i^3 \frac{2n_i - q_i - 1}{2q_i} \mathbf{b}_i, \quad (3.24)$$

where $n_i = 1, 2, \dots, q_i$ and which gives $q_1 \times q_2 \times q_3$ uniformly spaced k -points in the BZ.

If point symmetries of the BZ are employed, the k -point sampling can be restricted to the IBZ. A general function, such as the density, can be sampled in the IBZ as,^[67]

$$f_i = \frac{\Omega_0}{(2\pi)^3} \int_{\text{BZ}} d\mathbf{k} f_i(\mathbf{k}) = \sum_{\mathbf{k}}^{\text{IBZ}} w_{\mathbf{k}} f_i(\mathbf{k}) \quad (3.25)$$

where \mathbf{k} are irreducible set of the special k -points, (3.24), in the IBZ, which are weighted by the factors $w_{\mathbf{k}}$. These weight factors are given by ratio of the elements in the entire point group of the crystal to number of elements of the corresponding wave vector groups.

Choosing the grid for the k -point sampling is an important convergence parameter. While a function can be sampled faster on a smaller number of k -points, it is necessary to study that the quantity of interest is converged with respect to the size of the $q_1 \times q_2 \times q_3$ grid. This has to be done separately from studying the convergence with respect to the plane wave cut-off. In other words, for every chosen cut-off energy in the convergence study, the convergence with respect to different sets of k -points has to be studied as well.

3.2.5 Self-interaction error and the electron structure of InSb

It is well known that the local and semi-local approximations of XC in DFT fail to properly describe the energy gaps of insulators.^[62] As mentioned, for the present thesis this creates an obstacle as we are interested in simulating material parameters that describe electric field responses of polar optical phonons in the small band gap InSb. From literature, we already know that all electron calculations at LDA or GGA level of DFT describe InSb as a metal.^[76] However, in pseudopotential DFT this band gap problem can be avoided by the choice of pseudopotentials for In and Sb at the LDA level.

In section 3.2.2, we discussed that the Hartree potential in the KS equation, or in general, leads to the self-interaction of the electron with itself. We further showed that the exact orbital dependent exchange interaction cancels this. However, as in the LDA or GGA of DFT, the exchange is entirely approximated from the homogeneous electron gas

and the explicit dependence on the atomic orbital is lost. This leads to the SIE of DFT which is a major caveat of these approximate functionals. In particular, because of this the one-particle KS energies and orbitals are simply wrong. The question we ask here, with the present pseudopotential DFT, is that how wrong and for which atomic orbitals.

The one-particle energies given by KS equations are used to characterize the electronic band structures. In Fig. 5(a) is shown a KS band structure of InSb simulated with the Perdew-Wang LDA functional^[66] and scalar relativistic, (no spin-orbit coupling), pseudopotentials,^[77] using the plane wave DFT code ABINIT.^[78] These pseudopotentials consider the $4d^{10}5s^25p^1$ and $4d^{10}5s^25p^3$ electrons of In and Sb, respectively, and the remaining are frozen into the pseudopotential core. It is seen that indeed the gap is closed at Γ and LDA describes InSb as a metal for these pseudopotentials.

Looking at the band structure in (a) in more detail, the valence band maximum is given by a band which in the vicinity of the Γ point is rather flat in energy. As the band is flat, this implies that it arises from atomic orbitals with high degeneracy i.e., the five-fold degenerate 4d-orbitals of In and Sb. In these atomic orbitals the electrons are localized. The conduction band minimum is given by a band that close to the Γ point shows parabolic, free-electron like, dispersion. Therefore, it arises mainly from the delocalized 5s- and 5p-orbitals of In and Sb with smaller degeneracy.

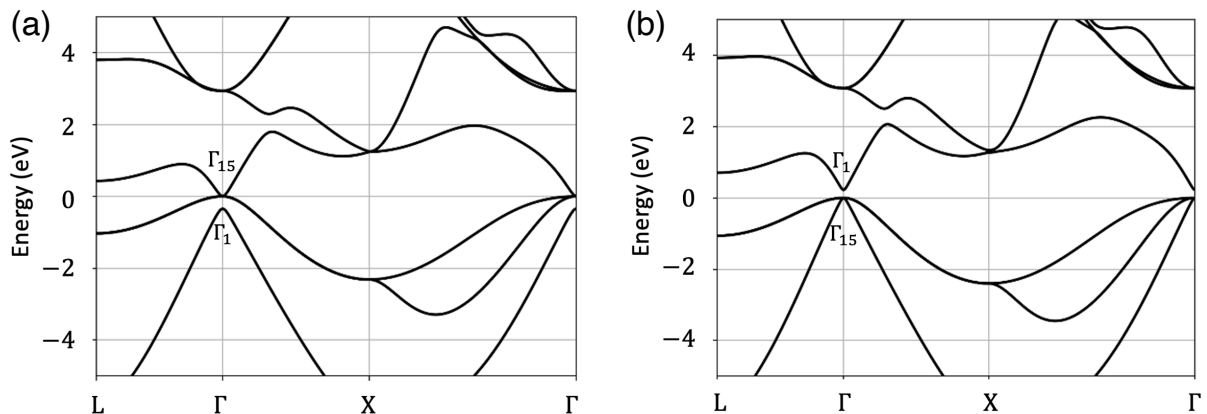


Figure 5: LDA KS band structures of InSb for two different scalar relativistic, (no spin-orbit coupling), pseudopotentials: (a) In and Sb 4d-orbitals in the valence of the pseudopotentials (b) In and Sb 4d-orbitals in the pseudopotential core. Freezing the 4d-orbitals of In into the pseudopotential core minimizes the self-interaction error of DFT in these localized orbitals, which pushes down the flat band at the valence band maximum resulting in a band gap of 0.22 eV.

The electrons in the homogeneous electron gas are more delocalized. Therefore, the SIE of DFT for delocalized electrons in the parabolic bands is well cancelled by the electron gas approximation of the XC. The vanishing of the band gap can be suggested to arise from the SIE in the flat band, corresponding to the localized electrons in the 4d-orbitals of In and Sb. This causes that the one-particle KS energies of this band are too high.

In Fig. 5(b) is shown a KS band structure simulated with the same Perdew-Wang LDA functional, but for scalar relativistic Hartwigsen-Goedecker-Hutter (HGH) pseudopotentials.^[79] In these pseudopotentials, the In and Sb 4d-electrons are frozen into the pseudopotential core, and only the $5s^25p^1$ and $5s^25p^3$ electrons of In and Sb, respectively,

are considered. It is seen that the flat band is now pushed down in energy and as a result gap of 0.22 eV opens at the Γ point. This is in good agreement with the experimental 0.235 eV gap.^[80] Therefore, the band gap problem of DFT in InSb at the LDA level can be avoided by minimizing the SIE in the localized 4d-orbitals of In and Sb by freezing these orbitals into the pseudopotential core. In particular, based on molecular orbital theory considerations of GaAs,^[81] we can suggest that it is the cation In 4d-orbitals that are located at the Fermi level of InSb and which close the gap due to the SIE. This is further verified by the fact that a similar band gap closing has been observed in InAs.^[82]

It is instructive to further note that the valence band maximum at Γ point of zincblende is the three-fold degenerate Γ_{15} irrep of the tetrahedral group T_d ,^[83] if the group of the electron spin is not considered. As described in Sec. 2.2.3, both the p-orbitals; (x, y, z) , and the three d-orbitals; (xy, yz, xz) , (where the remaining two d-orbitals are split by the tetrahedral crystal field), transform according to this irrep. This allows for coupling between the p- and d-orbitals at the Γ point.^[84] Therefore, the flat band will always be degenerate at Γ point with the one-particle energy of the parabolic conduction band as in (a) or the valence band as in (b) and never located in between. This further means that the ordering of the three-fold Γ_{15} and the one-fold s-orbital like Γ_1 states is wrong in (a).

Let us discuss the validity of our method for achieving the semiconductor properties of InSb for the DFPT simulations. In general, geometrical optimization using LDA functionals tends to underestimate the lattice constants.^[85] Furthermore, the geometrical optimization using the HGH pseudopotentials resulted in a 2% smaller lattice constant for InSb, due to the 4d-orbitals being frozen into the pseudopotential core. In comparison, using the pseudopotentials where the 4d-orbitals are considered as valence gave less than 1% smaller lattice constant. In general, smaller lattice constant implies higher vibrational frequencies^[86] and this choice can affect the accuracy of the DFPT simulated phonon dispersion. However, for a polar material where the LO-TO splitting can be described in terms of the dielectric constants, as will be shown in the upcoming section, and as the driving force of the harmonic oscillator model is based on electric field responses. It is better to optimize the simulations for the correct electronic structure over the geometry.

3.3 Density functional perturbation theory

The KS DFT is a ground state theory and the material parameters needed for the harmonic oscillator model are the response properties of InSb, which are not solved at the DFT level. However, these responses can be directly related to the changes of the total energy with respect to different perturbations, and which are solved at the DFPT level.

The general theoretical framework of DFPT is lengthy and as it inherits the practical aspects from DFT which we have already described. A review of the theory of DFPT is outside the scope of this thesis and we refer to the original papers by Gonze^[87–89] for the DFPT implementation in the ABINIT code. In this section, we will rather highlight the importance of considering the effect of the macroscopic electric field accompanied the longitudinal optical motion of ions in polar semiconductors for all the present simulations.

3.3.1 Phonons, linear and non-linear optics of polar semiconductors

In section 2.2 we described that the phonons are given by diagonalizing the dynamical matrix, (2.22), which in the harmonic approximation depends on the 2FC. This 2FC is given by the second order derivative of the crystal potential with respect to two atomic displacements. As the crystal potential contains an electronic and ionic contribution, the 2FC also contains these contributions,

$$\Phi_{l\alpha}^{\prime\prime\beta}(\mathbf{q}) = {}^{\text{el}}\Phi_{l\alpha}^{\prime\prime\beta}(\mathbf{q}) + {}^{\text{ion}}\Phi_{l\alpha}^{\prime\prime\beta}(\mathbf{q}). \quad (3.26)$$

In the framework of DFPT, the second derivative of electronic part of the potential energy can be calculated entirely from the first order derivatives of the KS orbitals and these orbitals are given by solving the Sternheimer equation.^[87] The ionic part, which does not depend on the electronic structure, can be calculated by the Ewald summation method. The explicit expressions for these two can be found given by Gonze and Lee.^[90]

As shown in appendix E, the Maxwell's equations of dielectric media describe that the LO motion of ions in polar materials is accompanied by a macroscopic electric field in the long wavelength limit. This field creates a restoring force on the ions and causes the LO mode to oscillate faster than the TO mode.^[12] This phenomenon is well known as the LO-TO splitting in polar materials. In addition, this electric field is also the reason for the strong Fröhlich coupling of the LO phonons as discussed in the introduction.

For first-principles calculations, this macroscopic electric field has to be considered in the Hamiltonian. However, care must be taken as this field is not lattice periodic.^[91] Therefore, the 2FC in the long wavelength limit is split as,^[90]

$$\Phi_{l\alpha}^{\prime\prime\beta}(\mathbf{q} \rightarrow 0) = {}^{\text{ana}}\Phi_{l\alpha}^{\prime\prime\beta}(\mathbf{q} = 0) + {}^{\text{nan}}\Phi_{l\alpha}^{\prime\prime\beta}(\mathbf{q} \rightarrow 0), \quad (3.27)$$

where the analytical part ${}^{\text{ana}}\Phi_{l\alpha}^{\prime\prime\beta}(\mathbf{q} = 0)$ does not contain the electric field and it is evaluated at the zone center as for non-polar material. The non-analytic part is,^[90]

$${}^{\text{nan}}\Phi_{l\alpha}^{\prime\prime\beta}(\mathbf{q} \rightarrow 0) = \frac{4\pi e^2}{\Omega_0} \frac{\sum_{\gamma} \hat{q}_{\gamma} Z_{l,\gamma\alpha}^* \sum_{\gamma'} \hat{q}_{\gamma'} Z_{l',\gamma'\beta}^*}{\sum_{\alpha\beta} \hat{q}_{\alpha} \varepsilon_{\alpha\beta}^{\infty} \hat{q}_{\beta}}, \quad (3.28)$$

where e is the elementary charge, Ω_0 is the volume of the primitive unit cell, \hat{q}_{γ} is a unit vector in direction γ and $Z_{l,\gamma\alpha}^*$ is the Born effective charge tensor of an atom l . $\varepsilon_{\alpha\beta}^{\infty}$ is the high frequency dielectric tensor, which describes the response of the material to an external electric field above the phonon resonance, but below the electronic band gap.

For the cubic InSb, the tensors are isotropic and the effective charges satisfy $Z_{\text{In}}^* = -Z_{\text{Sb}}^* = Z^*$ due to charge conservation. Inserting (3.28) into (3.27), the dynamical matrix in (2.21) gives the frequency of the LO mode based on the frequency of the TO mode as,

$$\omega_{\text{LO}}(\mathbf{q} \rightarrow 0) = \sqrt{\omega_{\text{TO}}(\mathbf{q} = 0)^2 + \frac{4\pi e^2}{\Omega_0} \frac{Z^{*2}}{\mu \varepsilon^{\infty}}}, \quad (3.29)$$

where μ is the reduced mass of InSb.

The dielectric tensor and the effective charges can both be related to the second order derivatives of the total energy,^[90] which are given by the first order derivatives of the KS

orbitals, and these orbitals can be solved from the Sternheimer equation.^[90] Therefore, provided that the band gap is correctly produced, DFPT gives a simple first-principles approach to evaluate the LO-TO splitting caused by the long-range Coulomb interactions between the ions in polar materials. In comparison, evaluating the derivatives of the crystal potential by simply displacing the atoms in a supercell geometry, the accurate description of this long-range interaction would require large supercells. This so-called finite difference method is computationally demanding for polar materials.

The LO-TO splitting only applies in the zone center limit, $\mathbf{q} \rightarrow 0$. At very small wave vectors, $q < \omega_{\text{LO}}/c$, where c is the speed of light, and at the exact zone center it should vanish.^[38] Achieving this would require to consider the fact that the Coulomb interaction between the ions is not instantaneous, as is assumed in non-relativistic theories, but rather travels with the speed of light. However, we do not consider relativistic effects in this work, as this condition is not satisfied for the THz radiation used to excite the LO phonon.

In DFPT, the Raman tensors for the TO modes are given by the third order derivative of the KS total energy with respect to two electric fields and displacement of an atom.^[92] For the Raman tensors of the LO modes, it is again necessary to consider the effect of the macroscopic field. This requires knowledge of the non-linear susceptibility and which is given by third order derivative of the KS energy with respect to three electric fields.^[92] Theorem in perturbation theory tells that $2n + 1$ order derivatives of the total energy can be evaluated from the n th order derivatives of the wave functions.^[67] This theorem has been imported to DFPT by Gonze and Vigneron^[93] and thanks to this, the Raman tensors can also be evaluated from the first order derivatives of the KS orbitals.

Finally, it is worth to note that the anharmonic lifetimes of phonons are also given by third order derivatives of the crystal potential. By the above $2n + 1$ theorem, these could also be evaluated from the first order derivatives of the KS orbitals. However, for the decay of the LO phonon in polar materials, the effect of the macroscopic electric should also be considered and this not available in DFPT at present.

4 Results and Discussion

In this section we will present the results for this thesis. First, we will discuss the DFPT simulated phonon dispersion of InSb and the LO phonon modes relevant for the THz excitation. We will further discuss the anharmonic decay of these modes to gain insight into the approximations made in the literature, and to gain a preliminary value for the lifetime to be used in the harmonic oscillator model. After this, we will discuss our results for the DFPT simulated linear and non-linear optical responses of InSb.

Equipped with the material parameters and an approximation for the anharmonic lifetime, we can solve the harmonic oscillator equations to model the TXRD intensity of the nearly forbidden reflections due to the THz excited LO phonons. We will discuss the intensity modulation of the different reflections for varying the THz pulse parameters and electric field polarizations. In the final section, we will present preliminary experimental results from the FemtoMAX beamline, which show that the nearly forbidden reflections can be clearly detected in the equilibrium geometry.

4.1 Longitudinal optical phonons in InSb for the THz excitation

In Fig. 6 is shown DFPT simulated phonon dispersion of InSb over a chosen \mathbf{q} -path along the IBZ. The phonon dispersion contains an acoustic band which consists of the three phonon branches that have zero frequency at the Γ point, as defined in the group theory section. The remaining three branches form the optic band. These two bands are separated by a phononic band gap, which can be defined as the separation between the dark blue acoustic and the red optic branch along $X - W - K$. Due to the small mass difference of In and Sb this phononic band gap is small.

In the phonon dispersion, the mode polarizations with respect to the underlying wave vectors have been denoted and the modes have also been characterized in terms of the irreps of their respective wave vector groups using the Koster notation,^[49] which can be found tabulated in appendix B. The longitudinal modes are higher in frequency than the transverse ones, except close to the BZ boundaries for the optical modes. Along the Δ and Λ directions, the transverse modes are two-fold degenerate and this degeneracy is lifted along the Σ direction due to small symmetry in this direction. This small symmetry causes that the Σ_1 phonons do not have definite polarizations, except in the $\mathbf{q} \rightarrow 0$ limit.

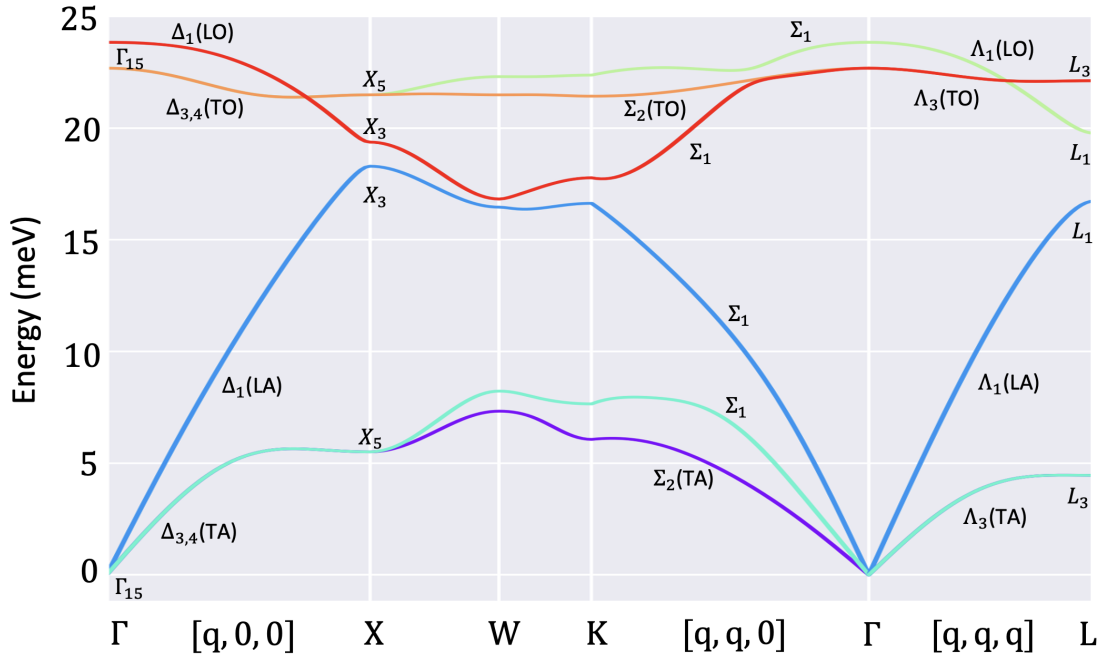


Figure 6: DFPT simulated phonon dispersion of InSb where the six different phonon branches of the zincblende structure have been labelled in terms of their irreps and mode polarizations.

In table 1 we have compared our simulated phonon frequencies to the experimental values measured by Price et al.^[94] with neutron diffraction for a selection of high symmetry points, (A and O stands for the points in the acoustic and optic bands, respectively). The phonon frequencies simulated in the harmonic approximation are seen to be in good agreement with the experimental values. However, for few acoustic modes at the BZ boundary points: $X_5(A)$, $L_1(A)$ and $L_3(A)$, our frequencies are slightly higher. We account this discrepancy to the choice of the soft LDA pseudopotentials, which underestimate the lattice constant by 2% and, therefore, overestimate the vibrational frequencies.

Table 1: DFPT simulated phonon frequencies for a selection of high symmetry points and experimental values measured by Price et al.^[94] with neutron diffraction at 300 K.

E/h (THz)	$\Gamma_{15}(\text{LO})$	$\Gamma_{15}(\text{TO})$	$X_5(\text{O})$	$X_3(\text{O})$	$X_3(\text{A})$	$X_5(\text{A})$	$L_3(\text{O})$	$L_1(\text{O})$	$L_1(\text{A})$	$L_3(\text{A})$
DFPT	5.77	5.49	5.20	4.67	4.42	1.33	5.35	4.78	4.05	1.08
Ref. ^[94]	5.90	5.54	5.38	4.75	4.30	1.12	5.31	4.82	3.81	0.98
(300 K)	± 0.25	± 0.05	± 0.17	± 0.20	± 0.10	± 0.05	± 0.06	± 0.10	± 0.06	± 0.05

The correct LO-TO splitting in polar semiconductors is in general more difficult to achieve with DFPT, as this depends on the dielectric properties and the band gaps are known to be underestimated by the local choices of exchange and correlation. In literature, the DFPT simulated LO branches of small band gap semiconductors can sometimes be noted to show camel back shaped dispersion centered at the Γ point.^[95] This is due to overestimating the high frequency dielectric constant in (3.28), due to too small band gap, and thus underestimating the LO-TO splitting. For the present method, we do not observe this camel back dispersion and from table 1 we can see that the difference between our $\Gamma_{15}(\text{LO})$ and $\Gamma_{15}(\text{TO})$ frequencies agree with the experimental². Therefore, our method works well for describing the LO-TO splitting, which is important for simulating the electric field responses of the polar optical phonons for the harmonic oscillator model.

For the present thesis, the phonon modes of interest for the THz excitation are the zone center limit, $\mathbf{q} \rightarrow 0$, LO phonons which have been visualized in Figs. 7(a-c). In (a) is shown $\Lambda_1(\text{LO})$ phonon, where the optical motion is longitudinal with respect to the x -direction, (or any other Cartesian direction). In (b) is shown a $\Sigma_1(\text{LO})$ phonon where the optical motion is longitudinal with respect to the $(x + y)$ -direction. (At finite wave vectors, Σ_1 phonons do not show definite polarizations and we have not denoted them in the phonon dispersion.) In (c) is shown a $\Lambda_1(\text{LO})$ phonon, where the optical motion is longitudinal in the $(x + y + z)$ -direction. In Figs. 2(a-b) in the introduction, the mode in (c) was shown to manifest itself in the large modulation of the XRD intensity of the nearly forbidden reflections. However, depending on the polarization of the THz radiation, we can excite these LO modes and we will later model their effect on the TXRD intensity.

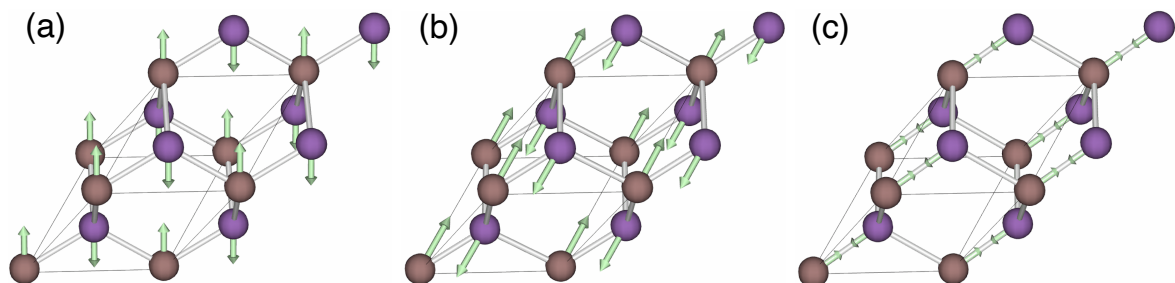


Figure 7: LO phonon modes of InSb in the zone center limit, $\mathbf{q} \rightarrow 0$: (a) $\Lambda_1(\text{LO})$ (b) $\Sigma_1(\text{LO})$ and (c) $\Lambda_1(\text{LO})$. The modes have been visualized using the phonon website.^[32]

²Based on group theory, the exact zone center Γ_{15} phonon is three-fold degenerate and the $\Gamma_{15}(\text{LO})$ and $\Gamma_{15}(\text{TO})$ frequencies in table 1 are referred in the zone center limit.

Let us discuss the anharmonic decay of these THz excited LO phonon modes. In Sec. 2.2.2 it was discussed that in the lowest and most dominant order, the anharmonic decay of the zone center LO phonon results in two phonons of opposite momenta, which together conserve the LO phonon energy. In section 2.2.1, it was further noted that the dynamical matrix satisfies time-reversal symmetry and thus the phonon branches at opposite momenta are identical. Therefore, the energy conservation in the decay can be evaluated for two phonon branches in a vertical line in the phonon dispersion.

Due to the LO-TO splitting and the small phononic band gap of InSb, various two phonon decay channels conserve the LO phonon energy. For example, the LO phonon can decay into a small wave vector TO phonon together with either a small wave vector LA or TA phonon, where the acoustic phonon compensates for the LO-TO split. This decay channel will be referred as the Ridley-Gupta channel.^[24] The energy of the LO phonon is also conserved by the decay into two identical acoustic phonons, each with approximately 12 meV energy in InSb, which is known as the Klemens channel.^[21] In addition, the LO phonon in InSb can also decay into two non-degenerate acoustic phonons, which will be referred as the Vallée-Bogani channel.^[22] In general, this Vallée-Bogani channel requires a smaller phononic band gap than the Klemens channel, and for InSb this channel conserves the LO phonon energy for two non-degenerate acoustic Σ_1 phonons close to the K point and for non-degenerate acoustic phonons on the path $X - W - K$ along the BZ boundary. As this Vallée-Bogani channel is allowed for InSb, it can be thought that the anharmonic lifetime of the LO phonon in InSb is small compared to other zincblende semiconductors.

As also discussed in Sec. 2.2.2, the coupling rate of the LO phonon with phonons in the different channels is distinguished by the anharmonic potentials (2.29). Based on the discussed analytical limit by Debernardi,^[11,43] it is directly concluded that the decay into the small wave vector optic and acoustic phonon in the Ridley-Gupta channel, should have small contributions to the anharmonic lifetime of the LO phonon. Furthermore, based on the fact that the approximated coupling rate favors two non-degenerate phonons over two degenerate phonons. It is suggested that the Vallée-Bogani channels dominate over the Klemens channels. Without considering the effect of the macroscopic field accompanied the LO phonon, Debernardi^[11] has found this to be true for GaAs. In particular, his DFPT data show that the single most dominating channel in GaAs is the decay into two non-degenerate acoustic Σ_1 phonons. This can be suggested to also be the case for InSb, as these two zincblende semiconductors have the same mass difference of the constituting atoms and thus a similar phonon dispersion and phononic band gap. It is noted, that the decays into non-degenerate acoustic phonons along BZ boundary $X - W - K$ do sum up to a large contribution to the anharmonic lifetime of the LO phonon in GaAs.^[11]

Above discussion contradicts the calculation of 7.26 ps LO phonon anharmonic lifetime in InSb at 300 K by Ferry^[25] under the assumption that the only decay channel is the Klemens channel. Thus, we will initially approximate the value of the LO phonon lifetime in our harmonic oscillator model as an average of the 6 ps lifetime determined from the Raman FWHM^[27] and the 10 ps lifetime measured by Lockwood et al.^[30] (It needs to be noted that the main result of Ferry is not the fact that he used the same approximation as Klemens did for calculating the LO phonon lifetime in silicon, but rather that Ferry showed that the polar nature of the LO has to be also considered for the decay in zincblende.)

4.2 Linear and non-linear optical responses of InSb

To model the oscillation amplitudes of the THz excited LO phonons using the harmonic oscillator model, we have simulated the Born effective charges for InSb with DFPT as: $Z_{\text{In}}^* = -Z_{\text{Sb}}^* = 2.03e$, where $-e$ is the electron charge. The sign difference of the effective charges can be directly justified by the fact that Sb is more electronegative than In, and, therefore, the Sb atoms form the anions in InSb. As we have shown that our choice of pseudopotentials for In and Sb correctly describes the LO-TO splitting, which depends on the Born effective charges via (3.29), we can further justify that the simulated Born effective charges are accurate. While experimental data on the Born effective charges are difficult to find, Asadi et al.^[96] have simulated the same values for the Born effective charges in InSb with DFPT. However, this is not surprising as their method for opening the band gap in InSb is by using the same LDA HGH pseudopotentials, where the In and Sb 4d-orbitals are frozen into the pseudopotential core, as ours.

For the elements of the Raman tensors we have simulated, $-d_{\text{In}} = d_{\text{Sb}} = 13.3 \text{ \AA}^{-1}$, (in SI units). As discussed in Sec. 3.3, the accuracy of these values can again be motivated by the fact that the LO-TO splitting and dielectric properties of InSb are correctly characterized by our choices of pseudopotentials. To the authors best knowledge, no experimental data on the Raman tensors of InSb exist in literature, and for comparison we rely on other DFPT simulations. Deinzer and Strauch^[97] have reported Raman polarizability, $\alpha = \Omega_0 |d_{\text{In}}| = 4\pi \times 70.5 \text{ \AA}^2$, (in SI units). If we use our theoretical volume of the primitive unit cell, $\Omega_0 = 63.9 \text{ \AA}^3$, our Raman polarizability is 4% smaller than the one simulated by Deinzer and Strauch. Using the experimental volume, $\Omega_0 = 68.0 \text{ \AA}^3$, our value is 2% larger. Deinzer and Strauch have not reported their volume or details of their method. Therefore, we can account this deviation to our small volume as a result of using the soft LDA HGH pseudopotentials, or them underestimating the band gap. Finally, we note that the Raman tensors have opposite signs with respect to the Born effective charges.

4.3 Time-resolved x-ray diffraction of THz excited LO phonons

Equipped with the DFPT simulated phonon modes and material parameters describing the linear and non-linear responses of InSb to external electric fields. We can finally solve the harmonic oscillator equations to model the TXRD intensity of the nearly forbidden reflections due to the THz excited LO phonons for a chosen THz pulse and polarization.

As discussed in Sec. 3.1, the electric field of an ultrashort pulse can be modelled to have a Gaussian envelope. Using Eq. (3.7), the electric field of an ultrashort THz pulse and its Gaussian envelope have been plotted in Fig. 8(a). The parameters for this pulse are: $\tau_{\text{FWHM}} = 200 \text{ fs}$, $\omega_{\text{THz}} = 2\pi \times 4.3 \text{ THz}$ and a total field strength of $|\mathbf{E}_0| = 1 \text{ MV/cm}$, which are reasonable THz parameters as can be generated from organic crystals. The pulse has been further centered at 1 ps. The spectral intensity of this pulse is also a Gaussian centered at $\omega_{\text{THz}} = 2\pi \times 4.3 \text{ THz}$ and its spectral FWHM is given by the time-bandwidth product: $\omega_{\text{FWHM}} = 2\pi \times 0.44/\tau_{\text{FWHM}} = 2\pi \times 2.2 \text{ THz}$. The normalized spectral intensity of the pulse in Fig. 8(a) has been plotted in Fig. 8(b).

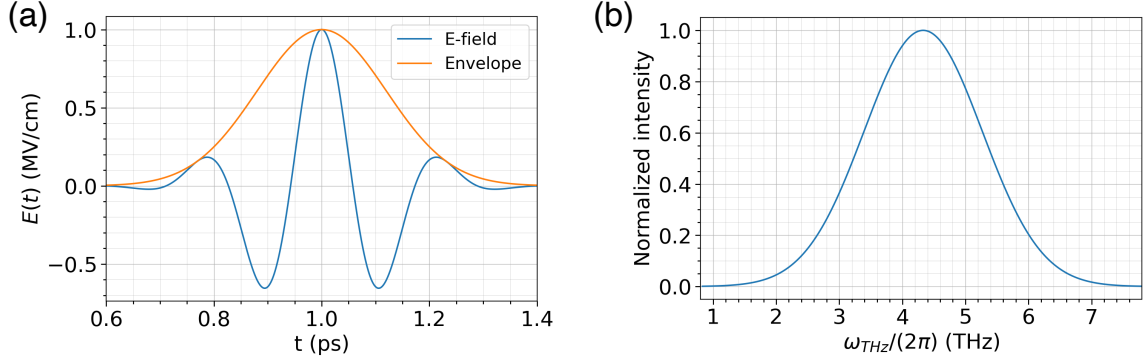


Figure 8: Ultrashort Gaussian THz pulse: (a) Electric field and its Gaussian envelope as function of time. (b) Normalized spectral intensity of the pulse in (a). Pulse parameters are: Carrier frequency; $\omega_{\text{THz}} = 2\pi \times 4.3$ THz, total field strength; $|\mathbf{E}_0| = 1$ MV/cm, temporal FWHM of the intensity of the pulse; $\tau_{\text{FWHM}} = 200$ fs and spectral FWHM; $\omega_{\text{FWHM}} = 2\pi \times 2.2$ THz.

As further described in Sec. 3.1, the forces due to the Raman terms which are quadratic in the fields, resonate at half the phonon frequency as a two photon sum-frequency Raman excitation. Therefore, we have initially chosen the carrier frequency of the pulse such that it contains equal amounts of the spectral component of the two photon Raman excitation frequency of InSb, $\omega_{\text{LO}}/2 = 2\pi \times 2.9$ THz and the dipole excitation frequency, $\omega_{\text{LO}} = 2\pi \times 5.8$ THz, approximately 30% as can be read from Fig. 8(b).

The Raman tensors were also noted to have opposite signs with respect to the Born effective charges. Therefore, the THz polarization has been initially chosen as, $E_{0x} = -E_{0y} = E_{0z} = |\mathbf{E}_0|/\sqrt{3}$. This results that the forces due to the terms quadratic in the fields are in the same direction as the forces due to the terms linear in the fields. This polarization excites LO phonon in the crystal $[1\bar{1}1]$ direction as was shown in Fig. 7(c).

For the above described THz pulse and polarization, solutions of the harmonic oscillator equations for displacements, $u_{\text{In},i}$, of the In atoms from their equilibrium positions in different Cartesian directions have been plotted in Figs. 9(a-c). The atoms can be seen to initially oscillate with the electric field of the pulse, centered at 1 ps, and the displacement in the y -direction is opposite to the displacement in the x - and z -directions. After the initial oscillation in the pulse, the oscillation of the atoms is sinusoidal, as described in (3.6), with frequency of the LO phonon $\omega_{\text{LO}} = 2\pi \times 5.8$ THz. This corresponds to a 170 fs period for the oscillation. Considering the peak at approximately 1.4 ps, which is the first peak after the initial oscillation in the pulse, the maximum displacement is 0.22 pm. This displacement then decays exponentially, $\exp[-t/(2\tau)]$, where the anharmonic lifetime of the LO phonon has been approximated as $\tau = 8$ ps based on the discussion in the end of Sec. 4.1.

Displacements of the Sb atoms in the zone center optical phonon mode are in the opposite directions scaled by the mass ratio of the atoms, $\mathbf{u}_{\text{Sb}} = -\sqrt{M_{\text{In}}/M_{\text{Sb}}}\mathbf{u}_{\text{In}}$. This gives approximately 0.3% change in the bond length between In and Sb. We also note that, even though the spectral intensities of the two photon Raman and the dipole excitation are equal for this THz pulse, only 1% of the displacement is due to the Raman terms.

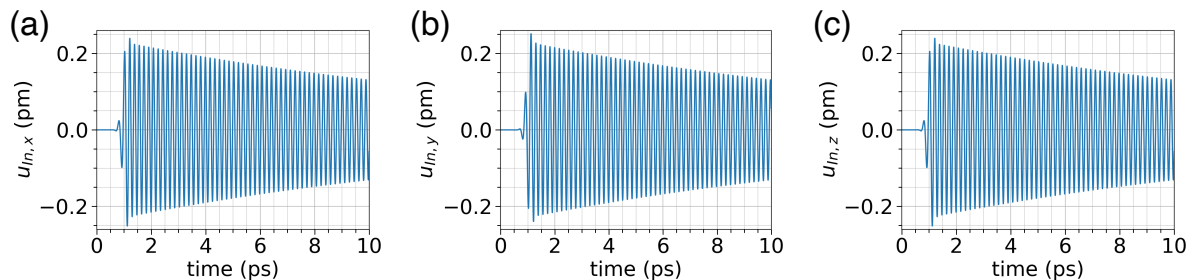


Figure 9: Displacements of In atoms in Cartesian directions according to the harmonic oscillator model driven by the ultrafast THz laser pulse defined in Fig. 8. After the initial oscillation in the electric field of the pulse centered at 1 ps, the amplitude of the LO phonon mode with frequency $\omega_{\text{LO}} = 2\pi \times 5.8$ THz decays exponentially, $\exp[-t/(2\tau)]$, where the anharmonic lifetime of the LO phonon in InSb has been approximated as $\tau = 8$ ps.

These displacements in the THz excited LO phonon can be inserted into the structure factor, (1.2), to model the TXRD intensity modulation. In Fig. 10(a) we have plotted the TXRD intensity of the nearly forbidden reflections, $\{2\bar{2}2, 222, 600, 200\}$, for InSb using the above defined THz pulse. The first few peaks arise from the initial oscillation of the atoms in the electric field of the pulse. Furthermore, as the TXRD intensity modulation is symmetric with respect to an increase or decrease of the bond length, an intensity maximum is observed twice per every oscillator period, i.e., every 85 fs. For THz polarization in the crystal $[1\bar{1}1]$ direction, the $2\bar{2}2$ reflection clearly shows the largest intensity modulation. Considering the intensity of the peak at approximately 1.4 ps, 50% increase in the intensity of the $2\bar{2}2$ reflection is observed. Furthermore, for the 8 ps approximation of the anharmonic lifetime of the LO phonon, approximately 10% increase of the intensity of this reflection can still be observed 12 ps after the THz pulse.

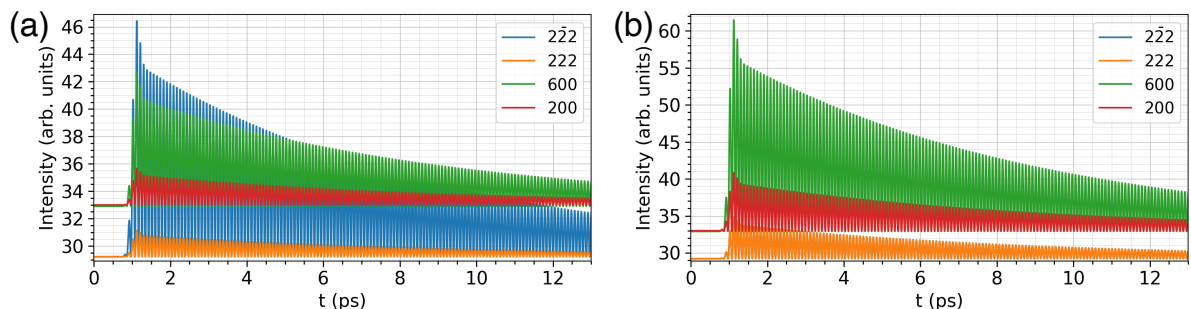


Figure 10: TXRD intensity of the nearly forbidden reflections of InSb for two different THz polarizations: (a) THz excitation of LO phonon in the crystal $[1\bar{1}1]$ direction, (b) THz excitation of LO phonon in the crystal $[100]$ direction. The THz pulse is described in Fig. 8

The intensity modulation of the reflections for the chosen THz polarization can be understood as follows. For displacing the atoms in one direction and not considering the periodicity caused by the phonon mode. The XRD intensity itself is a sinusoidal periodic function for the displacements, as given by the square modulus of the structure factor, (1.2), which takes the minimum value for the equilibrium positions of the atoms. (This

can be verified from Fig. 2(b) in the introduction, which would also show the periodicity if it was plotted for larger displacements.) Therefore, the maximum intensity modulation is achieved by maximizing the argument of the exponential in the structure factor: $(hu_{m,x} + ku_{m,y} + lu_{m,z})$, for the displacements $u_{m,i}$ due to the chosen THz polarization.

For THz polarization with all non-zero electric field components, reflections with all non-zero Miller indices are of interest. Furthermore, as the THz polarization used in Fig. 10(a) is specifically in the crystal $[1\bar{1}1]$ direction, the $2\bar{2}2$ reflection is the most modulated. In comparison, the negative displacement of the atoms in the y -direction counteracts the intensity modulation due to one of the two remaining positive displacements in the argument of the exponential for the 222 reflection. Therefore, the 222 reflection is significantly less modulated than the $2\bar{2}2$ reflection. If the THz polarization was instead in the crystal $[111]$ direction, these two reflections would be exchanged. However, with the distinction that for the $[111]$ THz polarization, the displacements due to the two photon Raman and dipole excitation are against each other. For the THz pulse used in (a), this effect is, however, negligible as 99% of the displacement comes from the terms linear in the fields.

Based on maximizing the argument of the exponential in the structure factor, the 600 reflection in Fig. 10(a) is more modulated than the 200 reflection, as the displacement in the x -direction is multiplied by six instead of two. However, there is no reason to probe either of these two reflections after exciting LO phonon mode in the diagonal crystal direction with all non-zero electric field components. Unless, the THz pulse is such that the forces due to the two photon Raman excitation, which requires a polarization with at least two non-zero electric field components, are dominating. Even still, the 600 reflection will not exceed the modulation of the $2\bar{2}2$ reflection for the $[1\bar{1}1]$ THz polarization.

In Fig. 10(b) is shown the intensity modulations of the nearly forbidden reflections for the same THz pulse as in Fig. 10(a), but for polarization $E_{0x} = |\mathbf{E}_0|$. This polarization results in LO phonon mode in the crystal $[100]$ direction, as was shown in Fig. 7(a), entirely as a dipole excitation. Clearly the 600 reflection is the most modulated and almost 70% increase in the intensity is observed. The reason why the 600 reflection is the most modulated can again be understood from maximizing the argument of exponential for displacements of the atoms only in the x -direction. We further note that the modulation of the 600 reflection in this polarization exceeds the modulation of the $2\bar{2}2$ reflection in (a), even though they both give the argument of the exponential to depend on the displacement as, $6u_{m,x}$. This is because the polarization $E_{0x} = |\mathbf{E}_0|$ in (b) gives 0.38 pm displacement in the x -direction, in comparison to the 0.22 pm displacement in (a).

While both the $2\bar{2}2$ and 600 reflection are clearly interesting to study after THz excitation of the LO phonon in the crystal $[1\bar{1}1]$ and $[100]$ direction, respectively. We will first given an overview of the effect of the different THz pulse parameters for the intensity modulation of the $2\bar{2}2$ reflection in the $[1\bar{1}1]$ polarization to understand their effect. Later, we will discuss in more detail the achievable intensity modulations of these two reflections for these two THz polarizations as a function of THz fields strengths.

In Figs. 11(a) and (b), we have studied the effect of the THz carrier frequency. In (a) the THz carrier frequency is $\omega_{\text{THz}} = 2\pi \times 4.3$ THz, which is the same as used Fig. 10(a), and in (b) the THz carrier frequency is $\omega_{\text{THz}} = 2\pi \times 3.8$ THz. Other pulse parameters are as defined in Fig. 8. It is seen that a significant drop in the intensity modulation is

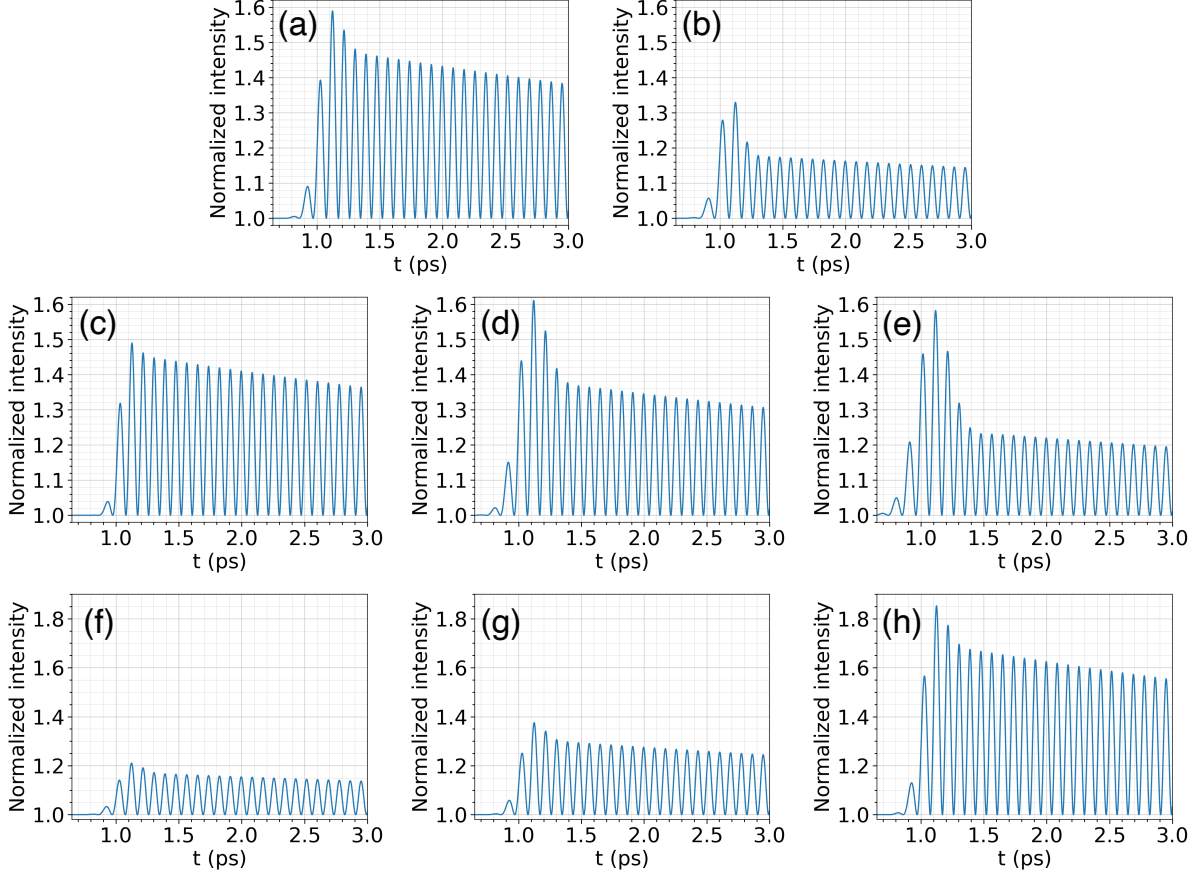


Figure 11: Comparison of the 222 reflection intensity modulation for THz polarization in the crystal $[1\bar{1}1]$ direction with respect to the different THz pulse parameters: Carrier frequency, ω_{THz} ; (a) $2\pi \times 4.3$ THz, (b) $2\pi \times 3.8$ THz. FWHM of the intensity of the pulse, τ_{FWHM} ; (c) 150 fs (d) 250 fs (e) 300 fs. Total field strength, $|\mathbf{E}_0|$; (f) 0.6 MV/cm (g) 0.8 MV/cm (h) 1.2 MV/cm. The other unspecified pulse parameters for each figure are as given in Fig. 8.

observed. This can be simply understood by shifting the center of the Gaussian spectral intensity in Fig. 8(b) by 0.5 THz to the left, and the pulse used in (b) only contains 10% of the dipole resonance component of the InSb LO phonon, as opposed to the 30% for the pulse used in (a). We note that, while the pulse centered at $\omega_{\text{THz}} = 2\pi \times 3.8$ THz in (b) now contains 50% of the two photon Raman frequency, the displacements due to the Raman terms are still only 4% of the total displacements for the 1 MV/cm field strength.

In Figs. 11(c-e) the effect of the temporal FWHM of the intensity of the pulse has been studied for $\tau_{\text{FWHM}} = [150, 250, 300]$ fs in (c), (d) and (e), respectively. Other pulse parameters are as defined in Fig. 8. It is seen that the shorter the FWHM is, the less the atoms initially oscillate in the pulse. The temporal FWHM also has a significant impact on the intensity modulation of the reflection after the initial oscillation. This is because the product of the temporal and spectral FWHMs for a Gaussian pulse is a constant, as described by the time-bandwidth product. Therefore, if the temporal FWHM increases, the spectral FWHM decreases, and a Gaussian pulse centered off resonance will contain less of the resonance component. In particular, the normalized spectral intensities of both

the two photon Raman and the dipole excitation are [50, 15, 6.5]% for pulses used in (c), (d) and (e), which explains the drop in the intensity modulation. However, the spectral intensity is also proportional to the square of the temporal FWHM,^[56] and we cannot precisely compare the normalized intensities of the spectral components for the different FWHMs. This effect can be observed, for example, by noting that in Fig. 11(c), with $\tau_{\text{FWHM}} = 150$ fs and 50% of the spectral intensity of the Raman and dipole excitation frequency. The increase in the intensity is still slightly smaller than previously in Fig. 11(a), where $\tau_{\text{FWHM}} = 200$ fs and the spectral intensities of these two components are 30%. While this suggests that pulses with large temporal FWHMs are favored, the coherent excitation of the LO phonon mode requires pulses with short duration.

In Figs. 11(f-h), we have compared the effect of the total field strength: $|\mathbf{E}_0| = [0.6, 0.8, 1.2]$ MV/cm in (f), (g) and (h), respectively. Other pulse parameters are as defined in Fig. 8. If we consider the intensity of the sixth peak at approximately 1.4 ps, we observe [18, 30, 47, 67]% increase in the intensity of the $2\bar{2}2$ reflection for the field strengths of $|\mathbf{E}_0| = [0.6, 0.8, 1.0, 1.2]$ MV/cm, where the value for $|\mathbf{E}_0| = 1.0$ MV/cm is taken from Fig. 11(a). As the intensity modulation is described by a sinusoidal periodic function, which takes the minimum value in the equilibrium. The modulation increases rapidly with increasing field strength and the corresponding atomic displacements.

The preceding discussion of the effect of the different pulse parameters on the TXRD intensity clearly highlights the significance of the phonon resonance component in the ultrashort pulse. However, it is still clear that significant increase in the XRD intensity can be achieved for ultrashort pulses even if they are not exactly centered at the phonon resonance. Equipped with this understanding, we will study the achievable intensity modulation of the reflections as a function of THz field strengths more systematically.

In Figs. 12(a-c) is shown the XRD intensity modulation of the nearly forbidden reflections in InSb as a function of the total field strength for three different THz carrier frequencies: (a) $\omega_{\text{LO}}/2 = 2\pi \times 2.9$ THz, (b) $\omega_{\text{LO}} = 2\pi \times 5.8$ THz and (c) $2\pi \times 3.5$ THz. The remaining pulse parameters are as defined in Fig. 8. The solid lines indicate the intensity modulations of the reflections for THz polarization: $[E_{0x}, E_{0y}, E_{0z}] = [1, -1, 1]|\mathbf{E}_0|/\sqrt{3}$ and the dashed lines are for THz polarization: $[E_{0x}, E_{0y}, E_{0z}] = [1, 0, 0]|\mathbf{E}_0|$. The values for the intensities have been taken as the maximum value of the TXRD peak at approximately 1.4 ps, which for the temporal FWHM of 200 fs is the first peak after the initial oscillation in the pulse. After this, the phonon mode decays exponentially.

Fig. 12(a) represents the two photon Raman excitation of the LO phonon mode with $\omega_{\text{THz}} = \omega_{\text{LO}}/2$. For this figure, we have artificially only considered the displacements due to the Raman terms and, as the Raman excitation requires at least two non-zero field components, the dashed lines have not been plotted since they are zero. We can see that the $2\bar{2}2$ reflection is the most modulated, as is expected for the $[1\bar{1}1]$ polarization, and 20% increase in the intensity can be achieved for a total field strength of 4.3 MV/cm. Clearly the two photon Raman excitation requires strong electric fields. However, it does give a degree of freedom to excite the LO phonon mode in zincblende entirely with THz radiation generated at half the phonon frequency. We remind that this two photon excitation is the method of choice for exciting large oscillation amplitudes of optical phonons in diamond structures, which are only Raman active, as has recently been demonstrated.^[53, 57]

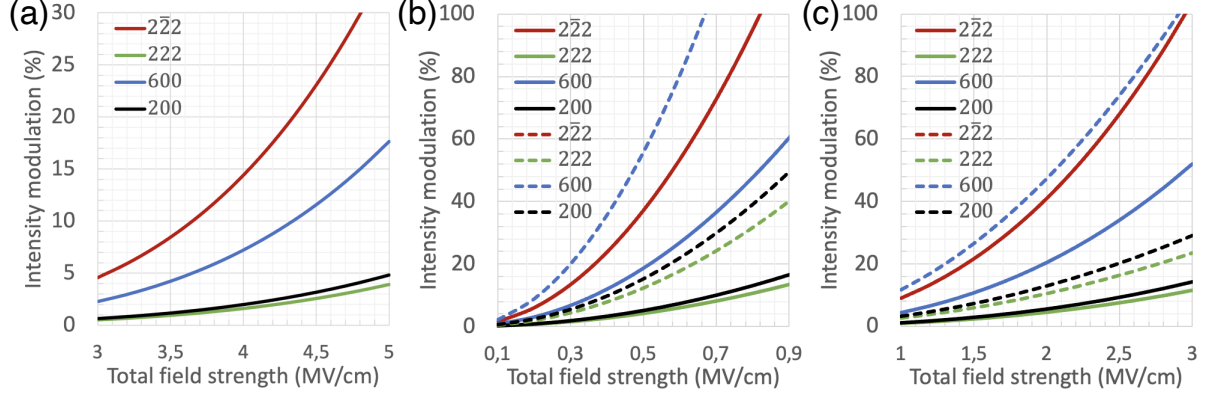


Figure 12: Maximum intensity modulations of the nearly forbidden reflections in InSb as a function of the total field strength of the THz pulse for three different carrier frequencies ω_{THz} : (a) $\omega_{\text{LO}}/2 = 2\pi \times 2.9$ THz (considering only the Raman terms, see text), (b) $\omega_{\text{LO}} = 2\pi \times 5.8$ THz and (c) $2\pi \times 3.5$ THz. The solid lines are intensity modulations for THz polarization; $[E_{0x}, E_{0y}, E_{0z}] = [1, -1, 1]|\mathbf{E}_0|/\sqrt{3}$ and dashed lines are for THz polarization; $[E_{0x}, E_{0y}, E_{0z}] = [1, 0, 0]|\mathbf{E}_0|$. Values for the intensity modulations have been taken as the value of the peak at 1.4 ps, which for 200 fs temporal FWHM is the first peak after the initial oscillation in the pulse. After this the phonon mode decays exponentially due to the anharmonic decay.

The reason why we have artificially only considered the displacements due to the Raman terms in (a) is that for InSb a pulse with temporal FWHM of 200 fs centered at the two photon Raman resonance, $\omega_{\text{LO}}/2 = 2\pi \times 2.9$ THz, contains 1% of the spectral component of the dipole resonance, $\omega_{\text{LO}} = 2\pi \times 5.8$ THz. This 1% dominates the intensity modulation via the terms linear in the fields until 3.5 MV/cm. Based on this, it is important to note that for THz polarization in the crystal [111] direction, where forces due to the Raman and linear terms are in the opposite directions. The pulse in (a), but for [111] polarization and considering the effect of both the linear and the Raman terms, results in less than 4% intensity modulation of the reflections for fields in range of 0 – 6 MV/cm. Therefore, this two photon Raman excitation at $\omega_{\text{LO}}/2$ in the [111] polarization should probably not be attempted for InSb or any other zincblende semiconductor where the frequencies $\omega_{\text{LO}}/2$ and ω_{LO} are not separated by many THz. This effect, however, becomes negligible if the pulse is moved towards the dipole resonance frequency, as will be discussed in the following, and the reflections show similar modulations in both [111] and $[1\bar{1}1]$ polarization, except the $2\bar{2}2$ is exchanged with 222.

Fig. 12(b) is the dipole excitation of the LO phonon mode with $\omega_{\text{THz}} = \omega_{\text{LO}}$. Clearly the 600 reflection in the [100] polarization is the most modulated and 20% increase in the intensity is already observed at a field strength of 0.3 MV/cm. For THz polarization in the crystal $[1\bar{1}1]$ direction the $2\bar{2}2$ is less modulated. This follows by the fact that for the [100] polarization the field component is $E_{0x} = |\mathbf{E}_0|$, while for the $[1\bar{1}1]$ polarization the field components are divided by $\sqrt{3}$, as discussed together with Fig. 10(b).

For THz radiation generated at the LO phonon frequency all the reflections show 20% increase in their intensity for fields below 1 MV/cm. Therefore, if THz radiation can be generated at the LO phonon frequency, it is possible to observe significant intensity

modulation for any of the reflections in InSb, in either [100], [111] or $[\bar{1}\bar{1}\bar{1}]$ polarizations. This gives great degree freedom for realizing the experimental setup.

The Born effective charges of III-V zincblende semiconductors are, in general, in the order of two elementary charges.^[11,91,96,98] Therefore, based on Fig. 12(b) it can also be suggested that significant intensity modulation of these reflections in any III-V should be possible to observe, if THz radiation can be generated close to their LO phonon frequencies. Even though InSb might be one of the better candidates, as the intensities of these reflections are very weak for the InSb equilibrium geometry, which is due to the small difference in the atomic form factors related to the difference in the atomic numbers. By which, large normalized intensity modulations are observed for small atomic displacements in InSb. These displacements are, however, normalized with respect to the lattice constant, which does make InSb the worst candidate of the III-V semiconductors.

THz radiation available at the FemtoMAX beamline is generated from organic DAST crystals. Referring to the spectrum generated by Vicario et al.,^[34] the DAST crystal shows broad emission between 0.1 – 10 THz and this spectrum consists of peaks at both the InSb dipole frequency, $\omega_{\text{LO}} = 2\pi \times 5.8$ THz and the two photon Raman frequency, $\omega_{\text{LO}}/2 = 2\pi \times 2.9$ THz. The intensity ratio of these frequencies is, $S(\omega_{\text{LO}})/S(\omega_{\text{LO}}/2) = 1/7$, where $S(\omega_{\text{LO}}/2)$ is very close to the global spectral maximum. The authors have further achieved peak field strengths of 6 MV/cm.

To model this spectrum by Vicario et al. quantitatively would require to extend the pulse beyond a single Gaussian. For example, into two Gaussians where one is centered at the $\omega_{\text{LO}}/2$ frequency and the other at ω_{LO} frequency and which are scaled by their relative intensities. Even though the present numerical method for solving the harmonic oscillators could be straightforwardly extended to consider pulses beyond a single Gaussian. We have not proceeded with this here as the spectrum for the present thesis depends specifically on what can be generated at the FemtoMAX beamline. Nevertheless, it can still be said that by using THz generated from the DAST organic crystals, the TXRD intensity modulation will be a combination of the two photon Raman and the dipole excitation.

In Fig. 12(c) the carrier frequency is $\omega_{\text{THz}} = 2\pi \times 3.5$ THz. This represents a single Gaussian pulse in the mixed case containing both the two photon Raman and the dipole excitation. It is seen that the modulation of the $\bar{2}\bar{2}\bar{2}$ reflection excited in the $[\bar{1}\bar{1}\bar{1}]$ polarization is close to the modulation of the 600 reflection excited in the [100] polarization. In the mixed case, the ordering of these two reflections depends on the ratio of the spectral intensities of the two photon Raman and the dipole frequency in the pulse. In other words, the intensity modulation of the $\bar{2}\bar{2}\bar{2}$ excited in the $[\bar{1}\bar{1}\bar{1}]$ polarization will exceed the 600 excited in the [100] polarization, if the excitation is more of the Raman type. Based on the spectrum generated by Vicario et al., which contains the ratio of these two spectral components, $S(\omega_{\text{LO}})/S(\omega_{\text{LO}}/2) = 1/7$, and which is more of the linear component than the pulse used in (c) where $S(\omega_{\text{LO}})/S(\omega_{\text{LO}}/2) = 1/16$. We can conclude that the linear terms dominate for the DAST spectrum. Therefore, for the maximum intensity modulation, the 600 excited in the [100] polarization would be the best probed for the DAST spectrum, or in general for the dipole excitation. The $\bar{2}\bar{2}\bar{2}$ in the $[\bar{1}\bar{1}\bar{1}]$ polarization is still, however, a very good candidate.

4.4 Preliminary experimental results from FemtoMAX

From the preceding section, it is clear that significant intensity modulation of the 600 or the $2\bar{2}2$ reflection can be observed for reasonable THz electric fields. However, this is only possible if these reflections can be clearly resolved in the equilibrium geometry.

In Figs. 13(a) and (b) is shown detection of the $2\bar{2}2$ reflection in the InSb equilibrium geometry at the FemtoMAX beamline. In Fig. 13(a), a scattering pattern representing a slice through the reciprocal space can be seen. The nearly forbidden $2\bar{2}2$ reflection is visible inside the area highlighted by the red rectangle. This image is a sum of 6000 x-ray pulses and the reflection is thus very weak. From theoretical studies, the ratio of diffracted photons between the $2\bar{2}2$ reflection and the 111 reflection is around 1/2500.

In Fig. 13(b) is shown the average number of diffracted photons from the $2\bar{2}2$ reflection per shot as a function of the incident x-ray energy, as detected inside the red rectangle region shown in (a). Based on the Bragg's law, the diffraction should be observed only at one energy, however, due to finite bandwidth of the x-rays the reflection can also be observed at slightly different energies. Nevertheless, the diffraction is clearly most pronounced at 6.73 keV, where 0.8 photons can be detected per x-ray pulse.

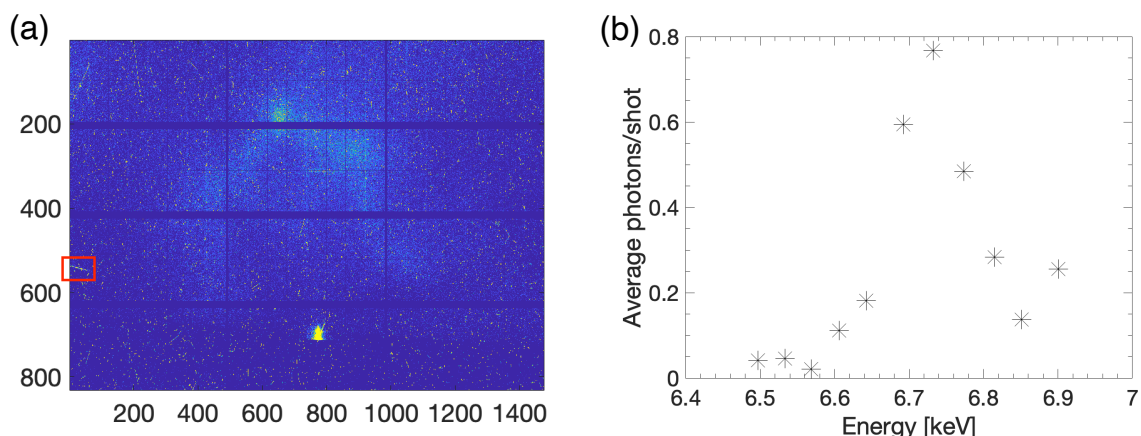


Figure 13: Nearly forbidden $2\bar{2}2$ reflection in InSb equilibrium geometry: (a) Image of the InSb reciprocal space and the observed $2\bar{2}2$ reflection inside the red rectangle. (b) Scan of the average number of diffracted photons from the $2\bar{2}2$ reflection per shot as a function of the x-ray energy.

From these figures, it can be concluded that the $2\bar{2}2$ reflection in the equilibrium geometry of InSb can be observed at FemtoMAX with a good resolution. The 0.8 average photons detected per x-ray pulse marks the equilibrium intensity in the simulated TXRD figures. Therefore, it should be possible to detect even a 20% increase in the intensity of this reflection after THz excitation of the LO phonon, and resolve its anharmonic lifetime from the decay of the intensity using the damped oscillator model.

5 Conclusion and Outlook

In the framework of an ultrafast THz pump, TXRD probe experiment, this thesis has consisted of a theoretical study on how TXRD can be used to measure anharmonic life-

times of LO phonons in polar zincblende semiconductors after an ultrashort THz pulse excitation. This technique has been made possible by identifying the existence of the nearly forbidden reflections in the zincblende structure, which show significant modulation of the XRD intensity already for sub-picometer atomic displacements. In the present thesis, displacement of the atoms in the THz excited LO phonon modes have been modelled with harmonic oscillator equations driven by electric fields of the THz radiation, and where the damping parameter is entirely determined by the anharmonic lifetime of the LO phonon. These equations have been solved numerically and their solutions give the TXRD intensity of the reflections via the phonon mode dependent structure factor.

The LO phonon in zincblende can be excited both as a two photon Raman excitation at half the phonon frequency and as a dipole excitation at the phonon frequency. Specializing the harmonic oscillator model for InSb, where the phonon modes and material parameters describing its response to external electric fields have been simulated from first-principles with DFPT. The theoretical TXRD intensity showed that the two photon Raman excitation of the LO phonon mode in the crystal $[\bar{1}\bar{1}1]$ direction with 200 fs Gaussian THz pulse centered at half the phonon frequency, results in 20% increase in the intensity of the $2\bar{2}2$ reflection at THz field strength of 4.3 MV/cm. In comparison, the dipole excitation of the LO phonon in the same crystal direction with a THz pulse centered at the phonon frequency, gave the same increase for the same reflection already at THz field strength of 0.4 MV/cm. Even larger intensity modulation can be observed by probing the 600 reflection after the dipole excitation of the LO phonon in the crystal $[100]$ direction, which for THz pulse centered at the LO phonon frequency resulted in the 20% increase at field strength of 0.3 MV/cm. However, realizing an experimental setup to probe the 600 reflection might require hard x-rays, as this reflection diffracts at significantly larger Bragg angles than the $2\bar{2}2$ reflection. Due to the anharmonic decay of the LO phonon significant TXRD intensity modulation should still be observable even 10 ps after the THz pulse. We have also argued that the anharmonic decay of the LO phonon most dominantly results in non-degenerate acoustic phonons close to the BZ boundary which conserves the energy due to the small phononic band gap of InSb, as opposed to the commonly assumed Klemens channel.

Based on these results, we can conclude that due to the dipole activity of the LO phonon in zincblende, significant intensity modulation of the nearly forbidden reflections is possible to observe with TXRD in zincblende semiconductors with achievable THz field strengths. The main requirement is that the THz radiation can be generated close to their LO phonon frequencies. In addition to directly observing the atomic motion in the THz excited LO phonon modes, this technique allows to determine the anharmonic lifetimes of these fundamental phonons in these polar semiconductors using the described damped harmonic oscillator model for the atomic displacements. Therefore, this thesis paves a way for a new ultrafast time-resolved technique to characterize anharmonic lifetimes of the LO phonons in different zincblende semiconductors. For which the data is at the present lacking, and which are needed as material parameters for modelling the carrier energy relaxations in the search of materials for hot carrier solar cells beyond the Shockley-Queisser limit.

References

- [1] M. V. Shugaev, C. Wu, O. Armbruster, A. Naghilou, N. Brouwer, D. S. Ivanov, T. J.-Y. Derrien, N. M. Bulgakova, W. Kautek, B. Rethfeld, *et al.*, “Fundamentals of ultrafast laser–material interaction,” *MRS Bulletin*, vol. 41, no. 12, pp. 960–968, 2016.
- [2] D. J. Flannigan and A. M. Lindenberg, “Atomic-scale imaging of ultrafast materials dynamics,” *MRS Bulletin*, vol. 43, no. 7, pp. 485–490, 2018.
- [3] A. M. Lindenberg, S. L. Johnson, and D. A. Reis, “Visualization of atomic-scale motions in materials via femtosecond x-ray scattering techniques,” *Annual Review of Materials Research*, vol. 47, pp. 425–449, 2017.
- [4] K. Sokolowski-Tinten, C. Blome, J. Blums, A. Cavalleri, C. Dietrich, A. Tarasevitch, I. Uschmann, E. Förster, M. Kammler, M. Horn-von Hoegen, and D. von der Linde, “Femtosecond x-ray measurement of coherent lattice vibrations near the lindemann stability limit,” *Nature*, vol. 422, pp. 287–289, Mar 2003.
- [5] D. A. Reis, M. F. DeCamp, P. H. Bucksbaum, R. Clarke, E. Dufresne, M. Hertlein, R. Merlin, R. Falcone, H. Kapteyn, M. M. Murnane, J. Larsson, T. Missalla, and J. S. Wark, “Probing impulsive strain propagation with x-ray pulses,” *Phys. Rev. Lett.*, vol. 86, pp. 3072–3075, Apr 2001.
- [6] J. Larsson, A. Allen, P. Bucksbaum, R. Falcone, A. Lindenberg, G. Naylor, T. Missalla, D. Reis, K. Scheidt, A. Sjögren, *et al.*, “Picosecond x-ray diffraction studies of laser-excited acoustic phonons in insb,” *Applied Physics A*, vol. 75, no. 4, pp. 467–478, 2002.
- [7] C. Ekström, *Acoustic, Thermal and Non-thermal Dynamics in Condensed Matter Studied by Time-Resolved X-ray Diffraction*. PhD thesis, 2020.
- [8] A. Lindenberg, I. Kang, S. L. Johnson, T. Missalla, P. Heimann, Z. Chang, J. Larsson, P. Bucksbaum, H. Kapteyn, H. Padmore, *et al.*, “Time-resolved x-ray diffraction from coherent phonons during a laser-induced phase transition,” *Physical review letters*, vol. 84, no. 1, p. 111, 2000.
- [9] A. H. Chin, R. W. Schoenlein, T. E. Glover, P. Balling, W. P. Leemans, and C. V. Shank, “Ultrafast structural dynamics in insb probed by time-resolved x-ray diffraction,” *Phys. Rev. Lett.*, vol. 83, pp. 336–339, Jul 1999.
- [10] C. Rose-Petruck, R. Jimenez, T. Guo, A. Cavalleri, C. W. Siders, F. Rksi, J. A. Squier, B. C. Walker, K. R. Wilson, and C. P. Barty, “Picosecond–milliångström lattice dynamics measured by ultrafast x-ray diffraction,” *Nature*, vol. 398, no. 6725, pp. 310–312, 1999.
- [11] A. Debernardi, “Phonon linewidth in iii-v semiconductors from density-functional perturbation theory,” *Phys. Rev. B*, vol. 57, pp. 12847–12858, May 1998.

- [12] M. Cardona and Y. Y. Peter, *Fundamentals of semiconductors*. Springer, 2005.
- [13] H. Fröhlich, “Interaction of electrons with lattice vibrations,” *Proceedings of the Royal Society of London. Series A. Mathematical and Physical Sciences*, vol. 215, no. 1122, pp. 291–298, 1952.
- [14] G. D. Mahan, *Many-particle physics*. Springer Science & Business Media, 2013.
- [15] P. Ruello and V. E. Gusev, “Physical mechanisms of coherent acoustic phonons generation by ultrafast laser action,” *Ultrasonics*, vol. 56, pp. 21–35, 2015.
- [16] D. W. Snoke, *Solid state physics: Essential concepts*. Cambridge University Press, 2020.
- [17] D. K. Ferry, “Non-equilibrium longitudinal optical phonons and their lifetimes,” *Applied Physics Reviews*, vol. 8, no. 2, p. 021324, 2021.
- [18] Y. Zhang, X. Jia, S. Liu, B. Zhang, K. Lin, J. Zhang, and G. Conibeer, “A review on thermalization mechanisms and prospect absorber materials for the hot carrier solar cells,” *Solar Energy Materials and Solar Cells*, vol. 225, p. 111073, 2021.
- [19] D. König, K. Casalenuovo, Y. Takeda, G. Conibeer, J. Guillemoles, R. Patterson, L. Huang, and M. Green, “Hot carrier solar cells: Principles, materials and design,” *Physica E: Low-dimensional Systems and Nanostructures*, vol. 42, no. 10, pp. 2862–2866, 2010. 14th International Conference on Modulated Semiconductor Structures.
- [20] S. Kahmann and M. A. Loi, “Hot carrier solar cells and the potential of perovskites for breaking the shockley–queisser limit,” *J. Mater. Chem. C*, vol. 7, pp. 2471–2486, 2019.
- [21] P. G. Klemens, “Anharmonic decay of optical phonons,” *Phys. Rev.*, vol. 148, pp. 845–848, Aug 1966.
- [22] F. Vallée and F. Bogani, “Coherent time-resolved investigation of lo-phonon dynamics in gaas,” *Phys. Rev. B*, vol. 43, pp. 12049–12052, May 1991.
- [23] B. K. Ridley, “The LO phonon lifetime in GaN,” *Journal of Physics: Condensed Matter*, vol. 8, pp. L511–L513, sep 1996.
- [24] B. K. Ridley and R. Gupta, “Nonelectronic scattering of longitudinal-optical phonons in bulk polar semiconductors,” *Phys. Rev. B*, vol. 43, pp. 4939–4944, Feb 1991.
- [25] D. K. Ferry, “Decay of polar-optical phonons in semiconductors,” *Phys. Rev. B*, vol. 9, pp. 4277–4280, May 1974.
- [26] M. Trigo, J. Chen, V. H. Vishwanath, Y. M. Sheu, T. Graber, R. Henning, and D. A. Reis, “Imaging nonequilibrium atomic vibrations with x-ray diffuse scattering,” *Phys. Rev. B*, vol. 82, p. 235205, Dec 2010.

- [27] W. Kiefer, W. Richter, and M. Cardona, “Second-order raman scattering in insb,” *Phys. Rev. B*, vol. 12, pp. 2346–2354, Sep 1975.
- [28] M. P. Marder, *Condensed matter physics*. John Wiley & Sons, 2010.
- [29] D. P. Edward and I. Palik, “Handbook of optical constants of solids,” 1985.
- [30] D. Lockwood, G. Yu, and N. Rowell, “Optical phonon frequencies and damping in alas, gap, gaas, inp, inas and insb studied by oblique incidence infrared spectroscopy,” *Solid State Communications*, vol. 136, no. 7, pp. 404–409, 2005.
- [31] H. Enquist, A. Jurgilaitis, A. Jarnac, Å. U. J. Bengtsson, M. Burza, F. Curbis, C. Disch, J. C. Ekström, M. Harb, L. Isaksson, M. Kotur, D. Kroon, F. Lindau, E. Mansten, J. Nygaard, A. I. H. Persson, V. T. Pham, M. Rissi, S. Thorin, C.-M. Tu, E. Wallén, X. Wang, S. Werin, and J. Larsson, “FemtoMAX – an X-ray beamline for structural dynamics at the short-pulse facility of MAX IV,” *Journal of Synchrotron Radiation*, vol. 25, pp. 570–579, Mar 2018.
- [32] H. Miranda, “Phonon website.”
<http://henriquemiranda.github.io/phononwebsite/phonon.html> [Accessed: 25-May-2021].
- [33] B. E. Warren, *X-ray Diffraction*. Courier Corporation, 1990.
- [34] C. Vicario, M. Jazbinsek, A. V. Ovchinnikov, O. V. Chefonov, S. I. Ashitkov, M. B. Agranat, and C. P. Hauri, “High efficiency thz generation in dstms, dast and oh1 pumped by cr:forsterite laser,” *Opt. Express*, vol. 23, pp. 4573–4580, Feb 2015.
- [35] J. Als-Nielsen and D. McMorrow, *Elements of modern X-ray physics*. John Wiley & Sons, 2011.
- [36] “Indium antimonide (insb), lattice parameter, thermal expansion: Datasheet from landolt-börnstein - group iii condensed matter · volume 41a1β: “group iv elements, iv-iv and iii-v compounds. part b - electronic, transport, optical and other properties” in springermaterials (https://doi.org/10.1007/10832182_378).”
 Copyright 2002 Springer-Verlag Berlin Heidelberg.
- [37] P. J. Brown, A. G. Fox, E. N. Maslen, M. A. O’Keefe, and B. T. M. Willis, *Intensity of diffracted intensities*, ch. 6.1, pp. 554–595. International Tables for Crystallography, 2006.
- [38] A. A. Maradudin and G. K. Horton, *Dynamical properties of solids*. New York, NY, 1974.
- [39] H. Ibach and H. Lueth, “Solid-state physics. an introduction to principles of materials science. 4. ed,” 2009.
- [40] N. W. Ashcroft, N. D. Mermin, *et al.*, *Solid state physics*, vol. 2005. holt, rinehart and winston, new york London, 1976.

- [41] P. Brüesch, *Phonons: Theory and experiments I: Lattice dynamics and models of interatomic forces*, vol. 34. Springer Science & Business Media, 2012.
- [42] J. Breeze, *Theory of Anharmonic Phonons*, pp. 111–133. Cham: Springer International Publishing, 2016.
- [43] A. Debernardi, “Anharmonic properties of semiconductors from density-functional perturbation theory,” 1995.
- [44] M. S. Dresselhaus, G. Dresselhaus, and A. Jorio, *Group theory: application to the physics of condensed matter*. Springer Science & Business Media, 2007.
- [45] P. W. Atkins and R. S. Friedman, *Molecular quantum mechanics*. Oxford university press, 2011.
- [46] F. Aryasetiawan, *Group Theory*. Lund University (unpublished), 2019.
- [47] J. Elliott and P. Dawber, *Symmetry in Physics, Volume 1 and 2*. Macmillan, 1979.
- [48] P. W. Atkins, M. S. Child, and C. S. G. Phillips, *Tables for group theory*, vol. 6. Oxford University Press Oxford, 1970.
- [49] G. Koster, “Space groups and their representations,” vol. 5 of *Solid State Physics*, pp. 173–256, Academic Press, 1957.
- [50] J. J. Sakurai and E. D. Commins, “Modern quantum mechanics, revised edition,” 1995.
- [51] M. Cardona, “Resonance phenomena,” *Light Scattering in Solids II*, pp. 19–178, 1982.
- [52] F. W. Byron and R. W. Fuller, *Mathematics of classical and quantum physics*. Courier Corporation, 2012.
- [53] S. Maehrlein, A. Paarmann, M. Wolf, and T. Kampfrath, “Terahertz sum-frequency excitation of a raman-active phonon,” *Phys. Rev. Lett.*, vol. 119, p. 127402, Sep 2017.
- [54] G. C. Cho, W. Kütt, and H. Kurz, “Subpicosecond time-resolved coherent-phonon oscillations in gaas,” *Phys. Rev. Lett.*, vol. 65, pp. 764–766, Aug 1990.
- [55] W. E. Bron, J. Kuhl, and B. K. Rhee, “Picosecond-laser-induced transient dynamics of phonons in gap and znse,” *Phys. Rev. B*, vol. 34, pp. 6961–6971, Nov 1986.
- [56] B. E. Saleh and M. C. Teich, *Fundamentals of photonics*. John Wiley & Sons, 2019.
- [57] D. M. Juraschek and S. F. Maehrlein, “Sum-frequency ionic raman scattering,” *Phys. Rev. B*, vol. 97, p. 174302, May 2018.
- [58] A. C. Hindmarsh and L. R. Petzold, “Lsoda, ordinary differential equation solver for stiff or non-stiff system,” Sep 2005.

- [59] P. Virtanen, R. Gommers, T. E. Oliphant, M. Haberland, T. Reddy, D. Cournapeau, E. Burovski, P. Peterson, W. Weckesser, J. Bright, S. J. van der Walt, M. Brett, J. Wilson, K. J. Millman, N. Mayorov, A. R. J. Nelson, E. Jones, R. Kern, E. Larson, C. J. Carey, Í. Polat, Y. Feng, E. W. Moore, J. VanderPlas, D. Laxalde, J. Perktold, R. Cimrman, I. Henriksen, E. A. Quintero, C. R. Harris, A. M. Archibald, A. H. Ribeiro, F. Pedregosa, P. van Mulbregt, and SciPy 1.0 Contributors, “SciPy 1.0: Fundamental Algorithms for Scientific Computing in Python,” *Nature Methods*, vol. 17, pp. 261–272, 2020.
- [60] L. Linnala, “Thesis-simulations.” <https://github.com/LassiL/Thesis-Simulations>, 2021.
- [61] M. Born and K. Huang, *Dynamical theory of crystal lattices*. Clarendon press, 1954.
- [62] J. P. Perdew, “Density functional theory and the band gap problem,” *International Journal of Quantum Chemistry*, vol. 28, no. S19, pp. 497–523, 1985.
- [63] P. Hohenberg and W. Kohn, “Inhomogeneous electron gas,” *Phys. Rev.*, vol. 136, pp. B864–B871, Nov 1964.
- [64] W. Kohn and L. J. Sham, “Self-consistent equations including exchange and correlation effects,” *Phys. Rev.*, vol. 140, pp. A1133–A1138, Nov 1965.
- [65] D. M. Ceperley and B. J. Alder, “Ground state of the electron gas by a stochastic method,” *Phys. Rev. Lett.*, vol. 45, pp. 566–569, Aug 1980.
- [66] J. P. Perdew and Y. Wang, “Accurate and simple analytic representation of the electron-gas correlation energy,” *Phys. Rev. B*, vol. 45, pp. 13244–13249, Jun 1992.
- [67] R. M. Martin, *Electronic structure: basic theory and practical methods*. Cambridge university press, 2020.
- [68] S. Baroni, S. de Gironcoli, A. Dal Corso, and P. Giannozzi, “Phonons and related crystal properties from density-functional perturbation theory,” *Rev. Mod. Phys.*, vol. 73, pp. 515–562, Jul 2001.
- [69] L. He, F. Liu, G. Hautier, M. J. T. Oliveira, M. A. L. Marques, F. D. Vila, J. J. Rehr, G.-M. Rignanese, and A. Zhou, “Accuracy of generalized gradient approximation functionals for density-functional perturbation theory calculations,” *Phys. Rev. B*, vol. 89, p. 064305, Feb 2014.
- [70] J. Heyd, G. E. Scuseria, and M. Ernzerhof, “Hybrid functionals based on a screened coulomb potential,” *The Journal of Chemical Physics*, vol. 118, no. 18, pp. 8207–8215, 2003.
- [71] Y.-S. Kim, K. Hummer, and G. Kresse, “Accurate band structures and effective masses for inp, inas, and insb using hybrid functionals,” *Phys. Rev. B*, vol. 80, p. 035203, Jul 2009.

- [72] V. I. Anisimov, F. Aryasetiawan, and A. I. Lichtenstein, “First-principles calculations of the electronic structure and spectra of strongly correlated systems: the lda + u method,” *Journal of Physics: Condensed Matter*, vol. 9, pp. 767–808, jan 1997.
- [73] F. Aryasetiawan and O. Gunnarsson, “The gw method,” *Reports on Progress in Physics*, vol. 61, no. 3, p. 237, 1998.
- [74] M. C. Payne, M. P. Teter, D. C. Allan, T. A. Arias, and J. D. Joannopoulos, “Iterative minimization techniques for ab initio total-energy calculations: molecular dynamics and conjugate gradients,” *Rev. Mod. Phys.*, vol. 64, pp. 1045–1097, Oct 1992.
- [75] H. J. Monkhorst and J. D. Pack, “Special points for brillouin-zone integrations,” *Phys. Rev. B*, vol. 13, pp. 5188–5192, Jun 1976.
- [76] J. Heyd, J. E. Peralta, G. E. Scuseria, and R. L. Martin, “Energy band gaps and lattice parameters evaluated with the heyd-scuseria-ernzerhof screened hybrid functional,” *The Journal of Chemical Physics*, vol. 123, no. 17, p. 174101, 2005.
- [77] M. van Setten, M. Giantomassi, E. Bousquet, M. Verstraete, D. Hamann, X. Gonze, and G.-M. Rignanese, “The pseudodojo: Training and grading a 85 element optimized norm-conserving pseudopotential table,” *Computer Physics Communications*, vol. 226, pp. 39–54, 2018.
- [78] X. Gonze, B. Amadon, G. Antonius, F. Arnardi, L. Baguet, J.-M. Beuken, J. Bieder, F. Bottin, J. Bouchet, E. Bousquet, N. Brouwer, F. Bruneval, G. Brunin, T. Cavignac, J.-B. Charraud, W. Chen, M. Côté, S. Cottenier, J. Denier, G. Geneste, P. Ghosez, M. Giantomassi, Y. Gillet, O. Gingras, D. R. Hamann, G. Hautier, X. He, N. Helbig, N. Holzwarth, Y. Jia, F. Jollet, W. Lafargue-Dit-Hauret, K. Lejaeghere, M. A. Marques, A. Martin, C. Martins, H. P. Miranda, F. Naccarato, K. Persson, G. Petretto, V. Planes, Y. Pouillon, S. Prokhorenko, F. Ricci, G.-M. Rignanese, A. H. Romero, M. M. Schmitt, M. Torrent, M. J. van Setten, B. Van Troeye, M. J. Verstraete, G. Zérah, and J. W. Zwanziger, “The abinitproject: Impact, environment and recent developments,” *Computer Physics Communications*, vol. 248, p. 107042, 2020.
- [79] C. Hartwigsen, S. Goedecker, and J. Hutter, “Relativistic separable dual-space gaussian pseudopotentials from h to rn,” *Phys. Rev. B*, vol. 58, pp. 3641–3662, Aug 1998.
- [80] I. Vurgaftman, J. R. Meyer, and L. R. Ram-Mohan, “Band parameters for iii–v compound semiconductors and their alloys,” *Journal of Applied Physics*, vol. 89, no. 11, pp. 5815–5875, 2001.
- [81] R. Cao, H.-X. Deng, J.-W. Luo, and S.-H. Wei, “Origin of the anomalous trends in band alignment of GaX/ZnGeX₂ (x = n, p, as, sb) heterojunctions,” *Journal of Semiconductors*, vol. 40, p. 042102, apr 2019.

- [82] Z. Zanolli, F. Fuchs, J. Furthmüller, U. von Barth, and F. Bechstedt, “Model *gw* band structure of *inas* and *gaas* in the wurtzite phase,” *Physical Review B*, vol. 75, no. 24, 2007.
- [83] B. S. Wherrett, *Group Theory for Atoms, Molecules, and Solids*. Prentice-Hall International, 1986.
- [84] S.-H. Wei and A. Zunger, “Calculated natural band offsets of all ii–vi and iii–v semiconductors: Chemical trends and the role of cation *d* orbitals,” *Applied Physics Letters*, vol. 72, no. 16, pp. 2011–2013, 1998.
- [85] C. Fiolhais, F. Nogueira, and M. A. Marques, *A primer in density functional theory*, vol. 620. Springer Science & Business Media, 2003.
- [86] J. A. Sanjurjo, E. López-Cruz, P. Vogl, and M. Cardona, “Dependence on volume of the phonon frequencies and the *ir* effective charges of several iii–v semiconductors,” *Phys. Rev. B*, vol. 28, pp. 4579–4584, Oct 1983.
- [87] X. Gonze, “Adiabatic density-functional perturbation theory,” *Phys. Rev. A*, vol. 52, pp. 1096–1114, Aug 1995.
- [88] X. Gonze, “Perturbation expansion of variational principles at arbitrary order,” *Phys. Rev. A*, vol. 52, pp. 1086–1095, Aug 1995.
- [89] X. Gonze, “First-principles responses of solids to atomic displacements and homogeneous electric fields: Implementation of a conjugate-gradient algorithm,” *Phys. Rev. B*, vol. 55, pp. 10337–10354, Apr 1997.
- [90] X. Gonze and C. Lee, “Dynamical matrices, born effective charges, dielectric permittivity tensors, and interatomic force constants from density-functional perturbation theory,” *Phys. Rev. B*, vol. 55, pp. 10355–10368, Apr 1997.
- [91] P. Giannozzi, S. de Gironcoli, P. Pavone, and S. Baroni, “Ab initio calculation of phonon dispersions in semiconductors,” *Phys. Rev. B*, vol. 43, pp. 7231–7242, Mar 1991.
- [92] M. Veithen, X. Gonze, and P. Ghosez, “Nonlinear optical susceptibilities, raman efficiencies, and electro-optic tensors from first-principles density functional perturbation theory,” *Physical Review B*, vol. 71, no. 12, p. 125107, 2005.
- [93] X. Gonze and J.-P. Vigneron, “Density-functional approach to nonlinear-response coefficients of solids,” *Phys. Rev. B*, vol. 39, pp. 13120–13128, Jun 1989.
- [94] D. L. Price, J. M. Rowe, and R. M. Nicklow, “Lattice dynamics of grey tin and indium antimonide,” *Phys. Rev. B*, vol. 3, pp. 1268–1279, Feb 1971.
- [95] L. Lindsay, D. A. Broido, and T. L. Reinecke, “Ab initio thermal transport in compound semiconductors,” *Phys. Rev. B*, vol. 87, p. 165201, Apr 2013.

- [96] Y. Asadi and Z. Nourbakhsh, “First principle characterization of structural, electronic, mechanical, thermodynamic, linear and nonlinear optical properties of zinc blende inas, insb and their inasxsb1-x ternary alloys,” *Journal of Physics and Chemistry of Solids*, vol. 132, pp. 213–221, 2019.
- [97] G. Deinzer and D. Strauch, “Raman tensor calculated from the $2n + 1$ theorem in density-functional theory,” *Phys. Rev. B*, vol. 66, p. 100301, Sep 2002.
- [98] S. de Gironcoli, S. Baroni, and R. Resta, “Piezoelectric properties of iii-v semiconductors from first-principles linear-response theory,” *Phys. Rev. Lett.*, vol. 62, pp. 2853–2856, Jun 1989.
- [99] M. I. Aroyo, A. Kirov, C. Capillas, J. M. Perez-Mato, and H. Wondratschek, “Bilbao Crystallographic Server. II. Representations of crystallographic point groups and space groups,” *Acta Crystallographica Section A*, vol. 62, pp. 115–128, Mar 2006.
- [100] A. H. Romero, D. C. Allan, B. Amadon, G. Antonius, T. Applencourt, L. Baguet, J. Bieder, F. Bottin, J. Bouchet, E. Bousquet, *et al.*, “Abinit: Overview and focus on selected capabilities,” *The Journal of chemical physics*, vol. 152, no. 12, p. 124102, 2020.
- [101] R. L. Graham, T. S. Woodall, and J. M. Squyres, “Open mpi: A flexible high performance mpi,” in *Parallel Processing and Applied Mathematics* (R. Wyrzykowski, J. Dongarra, N. Meyer, and J. Waśniewski, eds.), (Berlin, Heidelberg), pp. 228–239, Springer Berlin Heidelberg, 2006.
- [102] S. Goedecker, M. Teter, and J. Hutter, “Separable dual-space gaussian pseudopotentials,” *Phys. Rev. B*, vol. 54, pp. 1703–1710, Jul 1996.
- [103] J. Nocedal, “Updating quasi-newton matrices with limited storage,” *Mathematics of computation*, vol. 35, no. 151, pp. 773–782, 1980.
- [104] F. Aryasetiawan, *Electronic Structure Theory*. Lund University (unpublished), 2019.

Appendices

A Coefficients for the atomic form factors of In and Sb

Coefficients for the Gaussian parametrization of the atomic form factors in (2.13) for In and Sb have been tabulated in table 2.

Table 2: Coefficients for the Gaussian parametrization of the atomic form factors of In and Sb. Data from.^[37]

	a_1	b_1	a_2	b_2	a_3	b_3	a_4	b_4	c
In	19.1624	0.5476	18.5596	6.3776	4.2948	25.8499	2.0396	92.8029	4.9391
Sb	19.6418	5.3034	19.0455	0.4607	5.0371	27.9074	2.6827	75.2825	4.5909

B Group theory of zincblende

As discussed in the main text, the space group of zincblende InSb in different notations is: $(T_d^2, F\bar{4}3m, \#216)$, which consists of the group formed by the lattice translation vectors, $\{\mathbf{T}_n\}$, and the point group of a tetrahedron T_d . This tetrahedral point group consists of 24 symmetry operations (elements), G , in six different classes, C_k :

- e : the identity operation,
- $8C_3$: eight $\pm 2\pi/3$ rotations about the four body diagonals of the cube,
- $3C_2$: three rotations by π about the x, y, z axis,
- $6S_4$: six improper rotations by $\pm\pi/4$ about x, y and z axis followed by a reflection perpendicular to the axis of rotation,
- $6\sigma_d$: six reflections about the diagonal planes passing through the tetrahedral edges, formed by the lines $\{12, 13, 14, 23, 24, 34\}$.

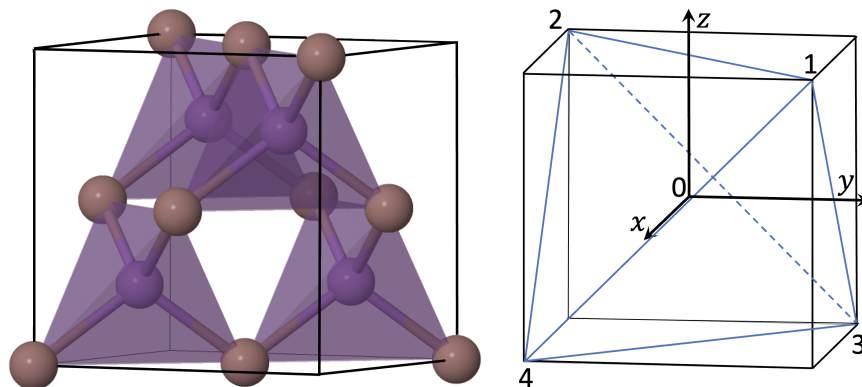


Figure 14: Symmetries of zincblende InSb (a) Tetrahedral symmetry of the primitive unit cell of the InSb crystal. (b) Visualization of the symmetry operations of the T_d group.

These operations transform the tetrahedron onto itself and form a mathematical group by satisfying the group axioms.^[47] They can also be conveniently visualized by placing one of the InSb tetrahedrons, shown in Fig. 14(a), inside a cube as shown in Fig. 14(b).

The effect of the symmetry operations of the T_d group on the Cartesian axes and the five atoms defined in Fig. 14(b) have been tabulated in table 3. This table also shows the effect of the symmetry operations on the products of the Cartesian basis (xy, yz, xz), which are given directly by multiplying the corresponding Cartesian columns together.

Table 3: Effect of the symmetry operations of T_d point group on Cartesian basis and atoms of a general tetrahedral AB_4 molecule

T_d	x	y	z	1	2	3	4	0	xy	yz	xz
e	x	y	z	1	2	3	4	0	xy	yz	xz
$C_3^+(1)$	z	x	y	1	3	4	2	0	zx	xy	zy
$C_3^-(1)$	y	z	x	1	4	3	2	0	yz	zx	yx
$C_3^+(2)$	$-z$	x	$-y$	3	2	4	1	0	$-zx$	$-xy$	zy
$C_3^-(2)$	y	$-z$	$-x$	4	2	1	3	0	$-yz$	zx	$-yx$
$C_3^+(3)$	z	$-x$	$-y$	4	1	3	2	0	$-zx$	xy	$-zx$
$C_3^-(3)$	$-y$	$-z$	x	2	4	3	1	0	yz	$-zx$	$-yx$
$C_3^+(4)$	$-z$	$-x$	y	2	3	1	4	0	zx	$-xy$	$-zy$
$C_3^-(4)$	$-y$	z	$-x$	3	1	2	4	0	$-yz$	$-zx$	yx
$C_2(x)$	x	$-y$	$-z$	4	3	2	1	0	$-xy$	yz	$-xz$
$C_2(y)$	$-x$	y	$-z$	3	4	1	2	0	$-xy$	$-yz$	xz
$C_2(z)$	$-x$	$-y$	z	2	1	4	3	0	xy	$-yz$	$-xz$
$S_4^+(x)$	$-x$	$-z$	y	3	1	4	2	0	xz	$-zy$	$-xy$
$S_4^-(x)$	$-x$	z	$-y$	2	4	1	3	0	$-xz$	$-zy$	xy
$S_4^+(y)$	z	$-y$	$-x$	2	3	4	1	0	$-zy$	yx	$-zx$
$S_4^-(y)$	$-z$	$-y$	x	4	1	2	3	0	zy	$-yx$	$-zx$
$S_4^+(z)$	$-y$	x	$-z$	4	3	1	2	0	$-yx$	$-xz$	yz
$S_4^-(z)$	y	$-x$	$-z$	3	4	2	1	0	$-yx$	xz	$-yz$
$\sigma_d(12)$	y	x	z	1	2	4	3	0	yx	xz	zy
$\sigma_d(13)$	z	y	x	1	4	3	2	0	zy	yx	zx
$\sigma_d(14)$	x	z	y	1	3	2	4	0	xz	zy	yx
$\sigma_d(23)$	x	$-z$	$-y$	4	2	3	1	0	$-xz$	zy	$-xy$
$\sigma_d(24)$	$-z$	y	$-x$	3	2	1	4	0	$-zy$	$-yx$	zx
$\sigma_d(34)$	$-y$	$-x$	z	2	1	3	4	0	yx	$-xz$	$-yz$

In representation theory, the elements, G , of the group are represented by square matrices $T(G)$ in a basis chosen for the rep. The rep can be characterized by the traces of

these matrices, and it can be shown that the symmetry operations belonging to the same class, C_k , have equal characters, in any rep.^[47] Therefore, the chosen rep can be entirely characterized by the traces of the matrices belonging to different classes of the group, i.e., $\chi(C_k) = \text{Tr}[T(C_k)]$.

From table 3 the characters of the matrix representations of the symmetry operations in various basis can be directly read. We have tabulated the characters of the classes of the T_d group in different basis in table 4, together with characters of the chosen direct product representations. Note that for general tetrahedral AB_4 molecule, the characters are given by the product of the characters of the Cartesian and the full atomic basis consisting of five atoms. For InSb the characters are given by multiplying the characters in the Cartesian representation by two, due to the translation group.

Table 4: Characters of the representations in different bases.

χ	e	$8C_3$	$3C_2$	$6S_4$	$6\sigma_d$
(x, y, z)	3	0	-1	-1	1
Atoms	5	2	1	1	3
AB_4	15	0	-1	-1	3
InSb	6	0	-2	-2	2
(xy, yz, xz)	3	0	-1	-1	1

The character table for the T_d group has been reproduced from the tables by Atkins et al.^[48] in table 5 using the Mulliken notation. By calculating the multiplicity as described in the main text, (2.31), the different reps in table 4 can be decomposed into direct sums of the irreps of the T_d group. In the table 5, we have noted that the rep relevant for the phonons at the Γ point of InSb reduces into $2T_2$. Furthermore, we have also identified that the Cartesian axes, (x, y, z) and their products (xy, yz, xz) have the same character as the T_2 irrep. Therefore, they transform as this irrep.

Table 5: Character table of the point group T_d in the Mulliken notation from Atkins et al.^[48] and the decomposition of the phonon rep for zincblende InSb.

T_d	e	$8C_3$	$3C_2$	$6S_4$	$6\sigma_d$	
A_1	1	1	1	1	1	
A_2	1	1	1	-1	-1	
E	2	-1	2	0	0	
T_1	3	0	-1	1	-1	
T_2	3	0	-1	-1	1	$(x, y, z), (xy, yz, xz)$
χ^{InSb}	6	0	-2	-2	2	$\chi = \sum_{\alpha} m_{\alpha} \chi^{\alpha} = 2T_2$

In table 6 we have tabulated the wave vector groups for the IBZ of the zincblende

structure shown in Fig. 15. The wave vector group at the Γ point is given by the entire point group of the real space lattice. The other wave vector groups in the IBZ are subgroups of the group at Γ , and these subgroups can be constructed by identifying the symmetry operations of the group at Γ that leave the wave vector invariant modulo reciprocal lattice vector, $T(G)\mathbf{k} = \mathbf{k} + \mathbf{G}_{hkl}$.

In table 6, we have also tabulated the decompositions of the phonon representations at the different wave vectors in the Mulliken notation. For convenience, we have also given the decompositions in the Koster notation.^[49] These decompositions can be determined by calculating the multiplicities, using Eq. (2.31) as described for the Γ point in the main text, but with respect to the characters of the classes of the corresponding wave vector group and their irreps. The characters of the classes of these wave vector groups for rep relevant for the phonons can also be identified from table 3. These irreps are then ordered to the phonon dispersion, Fig. 6, using the compatibility relations.^[44]

Table 6: Brillouin zone high symmetry paths and their wave vector groups.^[99] The decompositions of the InSb phonon representations in both Mulliken, for which the character tables can be found given by Atkins^[48] and also in Koster notation.^[49] $\xi = aq/(2\pi)$

Label	(q_x, q_y, q_z)	Group	Decomposition
Γ	$(0, 0, 0)$	T_d	$T_2(x, y, z) = \Gamma_{15}$
Δ	$(\xi, 0, 0)$	C_{2v}	$A_1(z) \oplus B_1(x) \oplus B_2(y) = \Delta_1 \oplus \Delta_3 \oplus \Delta_4$
X	$(1, 0, 0)$	D_{2d}	$B_2(z) \oplus E(x, y) = X_3 \oplus X_5$
W	$(1, 1/2, 0)$	S_4	$B(z) \oplus E(x, y)$
K	$(3/4, 3/4, 0)$	C_s	$2A'(x, y) \oplus A''(z)$
Σ	$\xi(3/4, 3/4, 0)$	C_s	$2A'(x, y) \oplus A''(z) = 2\Sigma_1 \oplus \Sigma_2$
Λ	(ξ, ξ, ξ)	C_{3v}	$A_1(z) \oplus E(x, y) = \Lambda_1 \oplus \Lambda_3$
L	$(1/2, 1/2, 1/2)$	C_{3v}	$A_1(z) \oplus E(x, y) = L_1 \oplus L_3$
$U = K$	$(3/4, 3/4, 0)$	C_s	$2A'(x, y) \oplus A''(z)$
Z	$(1, \xi/2, 0)$	C_2	$A(z) \oplus 2B(x, y)$
S	$(1, \xi/4, \xi/4)$	C_s	$2A'(x, y) \oplus A''(z)$
Q	$1/2(1 + \xi, 1, 1 - \xi)$	C_1	$3A_1$
q	(q_x, q_y, q_z)	C_1	$3A_1$

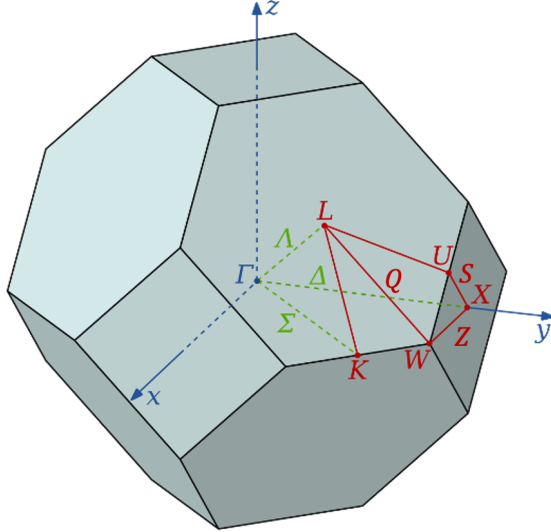


Figure 15: Brillouin zone of zincblende InSb

C Computational details for DFPT

The calculations for the zincblende InSb have been performed using the plane wave pseudopotential density functional perturbation theory (DFPT) code ABINIT^[78,100] in the framework of the local density approximation (LDA). These simulations were performed on a machine where the k -point sampling has been parallelized over four 3.2 GHz arm processor cores using open MPI.^[101] For the pseudopotentials, we have relied on the scalar relativistic norm-conserving Hartwigsen-Goedecker-Hutter (HGH) pseudopotentials,^[79] which have been constructed for the Goedecker-Teter-Huetter exchange-correlation functional.^[102] This reproduces the correlation functional by Perdew and Wang.^[66] In these HGH pseudopotentials, the 4d-orbitals of In and Sb are frozen into the pseudopotential core and only the three $5s^25p^1$ and five $5s^25p^3$ electrons of the In and Sb electrons, respectively, are considered. The calculations have been performed using theoretical lattice constant, which has been found by optimizing the geometry until the residual forces on the atoms are smaller than 0.5×10^{-5} Hartree/Bohr, using the limited-memory Broyden-Fletcher-Goldfarb-Shanno algorithm^[103] as implemented in ABINIT. This resulted in a lattice constant 2% smaller than the experimental, as is expected with LDA.

Freezing the In and Sb 4d-orbitals into the pseudopotential core gave an excellent agreement between the simulated Kohn-Sham band structure with 0.22 eV band gap at the Γ point and the experimental band gap of 0.235 eV,^[80] ignoring the effects of spin-orbit coupling. We have attempted further calculations using harder scalar relativistic PseudoDojo LDA pseudopotentials^[77] which also consider the 4d-orbitals of In and Sb. However, while these pseudopotentials improve the lattice constant, the system becomes metallic due to the self-interaction error in the localized 4d-orbitals of In.

We have used 25 Ha plane wave kinetic energy cut-off, which shows good convergence for the present soft HGH pseudopotentials. For the full phonon dispersion, in the harmonic approximation, and the Born effective charges, $4 \times 4 \times 4$ shifted Monkhorst and Pack grid^[75] of special k -points has been used. Due to the slower convergence of the Raman tensors,

$8 \times 8 \times 8$ shifted Monkhorst-Pack grid has been used instead.

D Exchange interaction in the homogeneous electron gas

Following Aryasetiawan^[104] and Martin,^[67] in this appendix we will formulate the exchange and correlation in terms of the pair distribution function and evaluate the exchange energy of the homogeneous electron gas as was given in (3.17) in the main text.

The total energy given by the many-body Hamiltonian (3.9) is,

$$E = \langle \Psi | \hat{H} | \Psi \rangle = \langle \hat{T} \rangle + \langle \hat{V}_{ee} \rangle + \int d^3r v_{\text{ext}}(\mathbf{r}) \rho(\mathbf{r}) + E_{\text{NN}}, \quad (5.1)$$

where the electron density is, $\rho(r) = N \int dr_2 \dots dr_N |\Psi(r, \dots, r_N)|^2$ with $r = (\mathbf{r}, \sigma)$ denoting both the position and the spin of an electron. The total energy can be entirely described based on the electron density. For the present discussion, it is of interest to discuss the expectation value of the electron-electron interaction term $\langle \hat{V}_{ee} \rangle$ in terms of the density.

Two particle density matrix is given by,

$$\begin{aligned} \Gamma^{(2)}(r, r') &= \langle \Psi | \hat{\rho}^{(2)}(r, r') | \Psi \rangle = \langle \Psi | \sum_{i \neq j} \delta(r - \hat{r}_i) \delta(r' - \hat{r}_j) | \Psi \rangle \\ &= N(N-1) \int dr_3 \dots dr_N |\Psi(r, r', \dots, r_N)|^2, \end{aligned} \quad (5.2)$$

where $\hat{\rho}^{(2)}(r, r')$ is the two-particle density operator.

Based on this, a normalized pair distribution function can be defined as,

$$g(r, r') = \frac{\Gamma^{(2)}(r, r')}{\rho(r)\rho(r')}. \quad (5.3)$$

This function describes the probability of finding one particle at \mathbf{r} with spin σ given that another particle is at \mathbf{r}' with spin σ' . For uncorrelated particles, the two particle density matrix is $\Gamma^{(2)}(r, r') = \rho(r)\rho(r')$ and the pair distribution equals to one.

The electron-electron interaction energy can then be written in terms of the pair distribution as,

$$\langle V_{ee} \rangle = \frac{1}{2} \int dr dr' \rho(r) \rho(r') v(r, r') + \frac{1}{2} \int dr dr' \rho(r) \rho(r') v(r, r') [g(r, r') - 1], \quad (5.4)$$

where $v(r, r') = 1/|\mathbf{r} - \mathbf{r}'|$. The first term in the above expression is the classical electrostatic energy as given by the Poisson's equation, i.e., the Hartree term. The second term is purely quantum mechanical known as the exchange and correlation. The term $\rho(r') [g(r, r') - 1]$ in the integrand is further called the exchange-correlation hole, which an electron r digs around it due to interactions with other electrons. Based on this, it can be interpreted that the quantum mechanical exchange and correlation is the Coulomb interaction of the electron with its hole.

The pair distribution of electrons in a homogeneous gas due to the exchange interaction between them can be evaluated analytically and it is approximated for the correlation.

The exchange interaction is defined to be given by the Hartree-Fock approximation. In this approximation, the many-body wave function Ψ of N electrons occupying states i is approximated by a single Slater determinant,

$$\Phi(r_1, \dots, r_N) = \frac{1}{\sqrt{N!}} \begin{vmatrix} \phi_1(r_1) & \dots & \phi_1(r_N) \\ \vdots & \ddots & \vdots \\ \phi_N(r_1) & \dots & \phi_N(r_N) \end{vmatrix} \quad (5.5)$$

where $\phi_i(r_j)$ are one-particle orbitals. As determinant changes sign when the rows or columns are interchanged, the Slater determinant satisfies the antisymmetry of the fermionic wave function under exchange of two identical fermions, as demanded by the Pauli exclusion principle.

The two particle density matrix in (5.2) can be written in second quantization as,

$$\Gamma^{(2)}(r, r') = \langle \Psi | \hat{\rho}^{(2)}(r, r') | \Psi \rangle = \sum_{ijkl} \rho_{ij,kl} \langle \Psi | c_i^+ c_j^+ c_l c_k | \Psi \rangle \quad (5.6)$$

where $\rho_{ij,kl} = \phi_i^*(r) \phi_j^*(r') \phi_k(r) \phi_l(r')$ and the fermion creation, c_i^+ , and annihilation operators, c_i , satisfy the anticommutator relations, $\{c_i, c_j\} = \{c_i^+, c_j^+\} = 0$ and $\{c_i^+, c_j\} = \delta_{ij}$.

Taking the wave function as a single Slater determinant, the above matrix element is non-zero only if $i \neq j$ and $l \neq k$, so either $i = k$ and $j = l$ or $i = l$ and $j = k$. The two non-zero matrix elements are then,

$$\begin{aligned} \langle \Psi | c_i^+ c_j^+ c_j c_i | \Psi \rangle &= \langle \Psi | c_j^+ c_j c_i^+ c_i | \Psi \rangle = 1, \\ \langle \Psi | c_i^+ c_j^+ c_i c_j | \Psi \rangle &= - \langle \Psi | c_i^+ c_i c_j^+ c_j | \Psi \rangle = -1. \end{aligned} \quad (5.7)$$

The two-particle density matrix in the Hartree-Fock approximation is then,

$$\Gamma^{(2)}(r, r') = \sum_{i \neq j}^{\text{occ}} \rho_{ij,ij} - \sum_{i \neq j}^{\text{occ}} \rho_{ij,ji}. \quad (5.8)$$

This gives the Hartree-Fock pair distribution as,

$$g_{\text{HFA}}^{\sigma\sigma'}(r, r') = \frac{\Gamma^{(2)}(r, r')}{\rho(r)\rho(r')} = 1 - \frac{|\sum_i^{\text{occ}} \phi_i(r) \phi_i^*(r')|^2}{\rho(r)\rho(r')}. \quad (5.9)$$

For an uniform non-magnetic electron gas where all the electrons are separated by $R = |\mathbf{r} - \mathbf{r}'|$ and the one-particle orbitals are taken as plane waves, $\phi_i(r) = \exp(i\mathbf{k}_i \cdot \mathbf{r}) \chi(\sigma) / \sqrt{V}$, where V is the volume of the gas and $\chi(\sigma)$ is the spin wave function. The pair distribution can be straightforwardly evaluated by changing the sum over the occupied states to an integral $\sum_{k < k_F} \rightarrow V/(2\pi)^3 \int d^3k$ and using spherical coordinates as,

$$g_{\text{HFA}}^{\sigma\sigma'}(r, r') = 1 - \left[\frac{3j_1(k_F R)}{k_F R} \right]^2 \delta_{\sigma, \sigma'} \quad (5.10)$$

where $j_1(k_F R)$ is the first order spherical Bessel function and the Fermi momentum is related to the density of electron gas as, $k_F^3 = 3\pi^2 \rho$. Inserting this into the second term of (5.4), straightforward integration of the Bessel function gives the exchange energy per electron per spin as,

$$\varepsilon_X(\rho) = \frac{E_X}{N} = -\frac{3}{4\pi} (3\pi^2 \rho)^{1/3}, \quad (5.11)$$

as described in (3.17) in the main text.

E Optical phonons in polar semiconductors

Following Ibach and Lüth^[39] and Marder,^[28] in this appendix we will show that the longitudinal optical motion of ions in polar materials is accompanied by a macroscopic electric field, which leads to the splitting of the LO and TO mode, as discussed throughout the thesis. This derivation involves treating the phonons in the ionic crystal using the Maxwell's equation of dielectric media. Several fundamental concepts are derived by this treatment, such as the dielectric function and the Lyddane–Sachs–Teller relation, which will also be described here.

In polar materials, such as InSb, it is important to consider the effect of the effective charges caused by the ionic bonding on the optical phonons. The separation \mathbf{Q} of the two ions in InSb can be modelled as a harmonic oscillator with reduced mass μ and a mode effective charge e^* in an external field as,

$$\mu[\ddot{\mathbf{Q}} + \gamma\dot{\mathbf{Q}} + \omega_0^2\mathbf{Q}] = e^*\mathbf{E}(t), \quad (5.12)$$

where γ describes the damping of the oscillator and ω_0 is the resonance frequency of the oscillator (or the phonon mode). This equation is readily solved by a Fourier transform,

$$\mathbf{Q}(\omega) = \frac{1}{\mu} \frac{e^*\mathbf{E}(\omega)}{\omega_0^2 - \omega^2 - i\gamma\omega}. \quad (5.13)$$

The polarization of the lattice consisting of n harmonic oscillators in an external field can be written as,

$$\mathbf{P}(\omega) = n[e^*\mathbf{Q}(\omega) + \varepsilon_0\alpha\mathbf{E}(\omega)], \quad (5.14)$$

where the first term in the parenthesis is the dipole moment due to the ionic motion and the second term describes the polarization due to redistribution of electrons in the electric field with a proportionality constant α .

In linear homogeneous media, the polarization in an external field is also given by,

$$\mathbf{P}(\omega) = \varepsilon_0\chi(\omega)\mathbf{E}(\omega), \quad (5.15)$$

where the frequency dependent susceptibility is related to the dielectric function as, $\chi(\omega) = \varepsilon(\omega) - 1$.

By writing out the dielectric function using (5.14) and (5.15) and defining the static dielectric constant ε^0 in the zero frequency limit and ε^∞ in the high frequency limit. The dielectric function of an ionic lattice consisting of harmonic oscillators can be written as,^[39]

$$\varepsilon(\omega) = \varepsilon^\infty + \omega_0^2(\varepsilon^0 - \varepsilon^\infty) \left[\frac{\omega_0^2 - \omega^2}{(\omega_0^2 - \omega^2)^2 + (\gamma\omega)^2} + i \frac{\gamma\omega}{(\omega_0^2 - \omega^2)^2 + (\gamma\omega)^2} \right]. \quad (5.16)$$

The dielectric function has been split to real and imaginary parts: $\varepsilon(\omega) = \varepsilon_1(\omega) + i\varepsilon_2(\omega)$, which are related to each other by the Kramers-Kronig relations.^[28] At resonance $\omega = \omega_0$ the real part is equal to the high-frequency dielectric constant, ε^∞ , and the imaginary part has a Lorentzian lineshape centered at resonance ω_0 , which indicates absorption. The FWHM of the Lorentzian is determined by the damping constant γ .

The square root of the dielectric function is equal to the complex refractive index, $\sqrt{\varepsilon(\omega)} = \tilde{n}(\omega) = n + i\kappa$, where n is the refractive index and κ is related to the absorption in the medium. In addition to the present discussion of phonons, this model dielectric function gives a way to fit the damping constant, arising from the many-body interactions in solids, by studying the refraction or absorption, as has been done by Palik^[29] and Lockwood et al.^[30] as reviewed in the introduction.

The Maxwell's equations of a dielectric non-magnetic media without free charges give the wave equation,^[28]

$$\vec{\nabla} \times \vec{\nabla} \times \mathbf{E}(\mathbf{r}, t) = -\mu_0 \frac{\partial^2 \mathbf{D}(\mathbf{r}, t)}{\partial t^2}, \quad (5.17)$$

where Fourier transform of the dielectric displacement field is $\mathbf{D}(\omega) = \varepsilon_0 \varepsilon(\omega) \mathbf{E}(\omega)$. Therefore, using $\nabla \times \nabla \times \mathbf{E} = \nabla(\nabla \cdot \mathbf{E}) - \nabla^2 \mathbf{E}$ and Fourier transforming with respect to both space and time we have in the long wavelength limit that,

$$q^2 \mathbf{E} - \mathbf{q}(\mathbf{q} \cdot \mathbf{E}) = \varepsilon(\omega) \frac{\omega^2}{c^2} \mathbf{E}, \quad (5.18)$$

where the electric field in the dielectric media can be described by,

$$\mathbf{E} = \mathbf{E}_0 e^{i(q\mathbf{e}_q \cdot \mathbf{r} - \omega t)}. \quad (5.19)$$

For a transverse wave, $\mathbf{q} \perp \mathbf{E}$, we find from (5.18) that $q = \sqrt{\varepsilon(\omega)} \frac{\omega}{c}$, which describes the absorption and refraction in the medium in terms of the dielectric function.

For a longitudinal wave, $\mathbf{q} \parallel \mathbf{E}$, (5.18) gives that $\varepsilon(\omega_{\text{LO}}) = 0$. Imposing this for the dielectric function in (5.16) and neglecting the damping γ , the LO frequency is given by,

$$\omega_{\text{LO}}^2 = \frac{\varepsilon^0}{\varepsilon^\infty} \omega_{\text{TO}}^2. \quad (5.20)$$

This is known as the Lyddane-Sachs-Teller relation, which describes that the LO phonon frequency is split from the TO phonon frequency by the ratio of the dielectric constants and which holds well experimentally.

Finally, from the Gauss law $\nabla \cdot \mathbf{D} = 0$ for the dielectric displacement field $\mathbf{D}(\mathbf{r}, t) = \varepsilon_0 \mathbf{E}(\mathbf{r}, t) + \mathbf{P}(\mathbf{r}, t)$ we get by Fourier transform in the long wavelength limit that,

$$\mathbf{q} \cdot [\varepsilon_0 \mathbf{E}(\mathbf{q}, t) + \mathbf{P}(\mathbf{q}, t)] = 0, \quad (5.21)$$

and we see that for the transverse modes $\mathbf{q} \perp \mathbf{E}$ the polarization is zero. However, for the longitudinal modes $\mathbf{q} \parallel \mathbf{E}$, there exists a macroscopic electric field,

$$\mathbf{E}_{\text{LO}} = -\frac{\mathbf{P}_{\text{LO}}}{\varepsilon_0} \propto \mathbf{Q}_{\text{LO}}, \quad (5.22)$$

where the polarization is proportional to the displacement by (5.14). This is a fundamental property of the LO mode separating it from the TO mode in the long wavelength limit as discussed in the main text. In addition to the LO-TO split, formulating this polarization in more detail leads also to the Fröhlich coupling in the polar materials.^[28]